

Co-Editor Decision: Publish subject to minor revisions (review by editor) (26 Jan 2019)  
by Luisa Molina

Comments to the Author:

Dear Authors,

I am pleased to accept your manuscript for publication after considering an additional comment from one of the referees, “In principle, all factors identified in the PMF analysis need to be independent of each other. However in the manuscript the 3rd factor is a derivative of other 4 factors. A more detailed clarification and/or explanation is needed.”

I would appreciate if you could respond to this comment.

Best regards, Luisa Molina

**Response:** Thanks very much for the editor’s kind decision. Following your suggestion, we changed the 3rd factor of “secondary particle formation” to “secondary source”, which should be independent from other primary sources identified in the manuscript. The Figure 4 and 5 were also modified accordingly.

# Impacts of short-term mitigation measures on PM<sub>2.5</sub> and radiative effects: case study at a regional background site near Beijing, China

Qiyuan Wang<sup>1\*</sup>, Suixin Liu<sup>1</sup>, Nan Li<sup>2</sup>, Wenting Dai<sup>1</sup>, Yunfei Wu<sup>3</sup>, Jie Tian<sup>4</sup>, Yaqing Zhou<sup>1</sup>, Meng Wang<sup>1</sup>, Steven Sai Hang Ho<sup>1</sup>, Yang Chen<sup>5</sup>, Renjian Zhang<sup>3</sup>, Shuyu Zhao<sup>1</sup>, Chongshu Zhu<sup>1</sup>, Yongming Han<sup>1,6</sup>, Xuexi Tie<sup>1</sup>, Junji Cao<sup>1,7\*</sup>

<sup>1</sup>Key Laboratory of Aerosol Chemistry and Physics, State Key Laboratory of Loess and Quaternary Geology, Institute of Earth Environment, Chinese Academy of Sciences, Xi'an, 710061, China.

<sup>2</sup>School of Environmental Science and Engineering, Nanjing University of Information Science & Technology, Nanjing, 210044, China

<sup>3</sup>Key Laboratory of Regional Climate-Environment Research for Temperate East Asia, Institute of Atmospheric Physics, Chinese Academy of Sciences, Beijing, 100029, China.

<sup>4</sup>Department of Environmental Science and Engineering, School of Energy and Power Engineering, Xi'an Jiaotong University, Xi'an 710049, China.

<sup>5</sup>Chongqing Institute of Green and Intelligent Technology, Chinese Academy of Sciences, Chongqing 400714, China.

<sup>6</sup>School of Human Settlements and Civil Engineering, Xi'an Jiaotong University, Xi'an, 710049, China.

<sup>7</sup>Institute of Global Environmental Change, Xi'an Jiaotong University, Xi'an, 710049, China.

Correspondence to: Qiyuan Wang (wangqy@ieecas.cn) and Junji Cao (cao@loess.llqg.ac.cn)

**Abstract.** Measurements at a background site near Beijing showed that pollution controls implemented during the 19th National Congress of the Communist Party of China (NCCPC) were effective in reducing PM<sub>2.5</sub>. Mass concentrations of PM<sub>2.5</sub> and its major chemical components were 20.6–43.1% lower during the NCCPC-control period compared with a non-control period, and differences were greater on days with stable meteorological conditions. A receptor model showed that PM<sub>2.5</sub> from traffic-related emissions, biomass burning, industrial processes, and mineral dust was 38.5–77.8% lower during the NCCPC-control versus non-control period, but differences in PM<sub>2.5</sub> from coal burning were small, and secondary source was higher during the control period. During one pollution episode in the non-control period, secondary source dominated, and the WRF-Chem model showed that the Beijing-Tianjin-Hebei (BTH) region contributed 73.6% of PM<sub>2.5</sub> mass. A second pollution episode was linked to biomass burning, and BTH contributed 46.9% of PM<sub>2.5</sub> mass. Calculations based on IMPROVE algorithms showed that organic matter was the largest contributor to light extinction during the non-control period whereas NH<sub>4</sub>NO<sub>3</sub> was the main contributor during the NCCPC. The Tropospheric Ultraviolet and Visible radiation model showed that the average direct radiative forcing (DRF) values at the Earth's surface were -14.0 and -19.3 W m<sup>-2</sup> during the NCCPC-control and non-control periods, respectively, and the DRF for the individual PM<sub>2.5</sub> components were 22.7–46.7% lower during the NCCPC. The information and dataset from this

删除的内容: particle formation

删除的内容: inorganic aerosol

37 study will be useful for developing air pollution control strategies in the BTH region and for  
38 understanding associated aerosol radiative effects.

## 39 **1 Introduction**

40 High loadings of fine particulate matter (PM<sub>2.5</sub>, particulate matter with an aerodynamic diameter ≤ 2.5  
41 μm) cause air quality to deteriorate (Pui et al., 2014; Tao et al., 2017), reduce atmospheric visibility  
42 (Watson, et al., 2002; Cao et al., 2012), and adversely affect human health (Feng et al., 2016; Xie et al.,  
43 2016). Moreover, PM<sub>2.5</sub> can directly and indirectly affect climate and ecosystems (Lecoeur et al., 2014;  
44 Tie et al., 2016). With the rapid increases in economic growth, industrialization, and urbanization in the  
45 past two decades, Beijing has experienced serious PM<sub>2.5</sub> pollution, especially in winter (e.g., Zhang et al.,  
46 2013; Elser et al., 2016; Wang et al., 2016a; Zhong et al., 2018). Since the Chinese government  
47 promulgated the National Ambient Air Quality Standards for PM<sub>2.5</sub> in 2012 (NAAQS, GB3095–2012), a  
48 series of emission control strategies have been implemented in Beijing and surrounding areas to alleviate  
49 the serious air pollution problems. These measures include installing desulphurization systems in coal-  
50 fired power plants, banning high-emission motor vehicles, and promoting natural gas as an alternative to  
51 coal in rural areas. According to the China Environmental State Bulletin  
52 ([www.zhb.gov.cn/hjzl/zghjzkgb/lnzghjzkgb](http://www.zhb.gov.cn/hjzl/zghjzkgb/lnzghjzkgb), in Chinese), the annual levels of PM<sub>2.5</sub> during 2013–2016 in  
53 Beijing showed a decreasing trend ( $r = 0.98$  and slope =  $-5.3 \mu\text{g m}^{-3} \text{ year}^{-1}$ ), but there were still 45.9% of  
54 days in 2016 that suffered from varying degrees of pollution.

55 Identifying the causes of air pollution in Beijing is challenging because the chemical composition of PM<sub>2.5</sub>  
56 is variable and complex, and the particles originate from a variety of sources and processes. For example,  
57 Elser et al. (2016) reported that organic aerosol (OA) was the largest contributor to PM<sub>2.5</sub> mass during  
58 extreme haze periods in Beijing, and the primary aerosol from coal combustion (46.8%) was the dominant  
59 contributor to OA, followed by the oxygenated OA (25.0%) and biomass burning OA (13.8%). In addition,  
60 Zheng et al. (2016) found that organic matter (OM) was the most abundant component (18–60%) in PM<sub>2.5</sub>,  
61 but its relative contribution usually decreased as pollution levels rose while those of secondary inorganic  
62 species (e.g., sulfate and nitrate) increased.

63 In recent years, the Chinese government has taken temporary control measures to ensure good air quality  
64 during some important conferences and festivals held in Beijing, including the 2008 Summer Olympic  
65 Games, the 2014 Asia-Pacific Economic Cooperation (APEC) summit, and the 2015 Victory Day parade  
66 (VDP). These actions provide valuable opportunities for evaluating the effectiveness of emission controls

67 on air pollution, and the information gathered during the control periods should be useful for making policy  
68 decisions. Numerous studies have demonstrated that temporary aggressive control measures were  
69 effective in reducing primary pollutants and secondary aerosol formation in Beijing (e.g., Wang et al.,  
70 2010; Guo et al., 2013; Li et al., 2015; Tao et al., 2016; Xu et al., 2017).

71 Air pollution in Beijing is not only influenced by local emissions and the regional transport of pollutants  
72 but also by meteorological conditions (e.g., Li and Han, 2016; Bei et al., 2017). In this regard, Zhong et  
73 al. (2018) concluded that heavy pollution episodes in Beijing can be generally divided into two phases (1)  
74 a transport stage, which is characterized by increases in pollutants mainly transported from the south of  
75 Beijing and (2) an accumulation stage, during which there is dramatic growth in PM<sub>2.5</sub> loadings due to  
76 stagnant meteorological conditions. Moreover, several studies ~~showed that the emission controls put in~~  
77 place during important events were effective in decreasing aerosol concentrations, but meteorological  
78 conditions also played an important role in determining aerosol loadings (Gao et al., 2011; Liang et al.,  
79 2017). For example, Liang et al. (2017) ~~found that meteorological conditions and emission control~~  
80 measures had comparable impacts on PM<sub>2.5</sub> loadings in Beijing during the 2014 APEC (30% versus 28%,  
81 respectively) and the 2015 VDP (38% versus 25%).

82 The existing studies on the effects of temporary air pollution controls in Beijing have not covered mid-  
83 autumn when meteorological conditions are typically complex and variable. Indeed, Zhang et al. (2018)  
84 reported that two weather patterns common in October caused heavy pollution episodes in Beijing. One  
85 episode was linked to a Siberian high-pressure system and a uniform high-pressure field while the second  
86 was associated with a cold front and a low-pressure system. For this study, measurements were made at  
87 a regional background site in the Beijing-Tianjin-Hebei (BTH) region to investigate the changes of PM<sub>2.5</sub>  
88 during the 19th National Congress of the Communist Party of China (NCCPC), which was held in Beijing  
89 from 18–24 October. Temporary control measures were implemented in Beijing and neighboring areas;  
90 these included restrictions on the number of vehicles, prohibition of construction activities, and  
91 restrictions on factories and industrial production. The primary objectives of this study were to (1)  
92 investigate the effectiveness of emission control measures on PM<sub>2.5</sub> and the associated changes in its  
93 chemical composition; (2) determine the contributions of emission sources to PM<sub>2.5</sub> mass during the  
94 NCCPC-control and non-control periods; and (3) evaluate the impacts of reductions of PM<sub>2.5</sub> on aerosol  
95 direct radiative forcing (DRF) at the Earth's surface. The study produced a valuable dataset and the results  
96 provide insights into how controls on air pollution can affect Beijing.

删除的内容: have shown

删除的内容: have

## 99 **2 Materials and methods**

### 100 **2.1 Sampling site**

101 Intensive measurements were made from 12 October to 4 November 2017 at the Xianghe Atmospheric  
102 Observatory (39.75° N, 116.96° E; 36 m above sea level) to investigate how the characteristics of PM<sub>2.5</sub>  
103 and the associated radiative effects were affected by the controls put in place during the NCCPC. Xianghe  
104 is a small county with 0.33 million residents, and it is located in a major plain-like area ~50 km southeast  
105 from Beijing and ~70 km north from Tianjin (Figure 1). The sampling site is surrounded by residential  
106 areas and farmland, and it is ~5 km west of Xianghe city center. This regional aerosol background site is  
107 influenced by mixed emission sources in the BTH region. A more detailed description of the site may be  
108 found in Ran et al. (2016).

### 109 **2.2 Measurements**

#### 110 **2.2.1 Offline measurements**

111 PM<sub>2.5</sub> samples were collected on 47 mm quartz-fiber filters (QM/A; GE Healthcare, Chicago, IL, USA)  
112 and Teflon® filters (Whatman Limited, Maidstone, UK) using two parallel mini-volume samplers  
113 (Airmetrics, Oregon, USA) that operated at a flow rate of 5 L min<sup>-1</sup>. The duration of sampling was 24 h,  
114 and the sampling interval was from 09:00 local time to 09:00 the next day. To minimize the evaporation  
115 of volatile materials, the samples were stored in a refrigerator at -4 °C before the chemical analyses. The  
116 quartz-fiber filters were used for determinations of water-soluble inorganic ions and carbonaceous species  
117 while the Teflon® filters were used for inorganic elemental analyses. The PM<sub>2.5</sub> mass on each sample  
118 filter was determined gravimetrically using a Sartorius MC5 electronic microbalance with ± 1 µg  
119 sensitivity (Sartorius, Göttingen, Germany). For the mass determinations, the filters were equilibrated  
120 under controlled temperature (20–23 °C) and relative humidity (35–45%) before the measurements were  
121 made. Field blanks (a blank quartz-fiber filter and a blank Teflon® filter) were collected and analysed to  
122 account for possible background effects.

123 Water-soluble inorganic ions, including F<sup>-</sup>, Cl<sup>-</sup>, NO<sub>3</sub><sup>-</sup>, SO<sub>4</sub><sup>2-</sup>, Na<sup>+</sup>, K<sup>+</sup>, Mg<sup>2+</sup>, Ca<sup>2+</sup>, and NH<sub>4</sub><sup>+</sup> were  
124 measured with the use of a Dionex 600 ion chromatograph (IC, Dionex Corp., Sunnyvale, CA, USA).  
125 The four anions of interest were separated using an ASII-HC column (Dionex Corp.) and 20 mM  
126 potassium hydroxide as the eluent. The five cations were separated using a CS12A column (Dionex) and  
127 an eluent of 20 mM methane sulfonic acid. More detailed description of the IC analyses may be found in  
128 Zhang et al. (2011). Carbonaceous species, including organic carbon (OC) and elemental carbon (EC)

129 were determined using a Desert Research Institute (DRI) Model 2001 thermal/optical carbon analyzer  
130 (Atmoslytic Inc., Calabasa, CA, USA) following the Interagency Monitoring of Protected Visual  
131 Environments (IMPROVE\_A) protocol (Chow et al., 2007). A standard sucrose solution was used to  
132 establish a standard carbon curve before the analytical runs. Replicate analyses were performed at a rate  
133 of one sample for every ten samples, and the repeatability was found to be < 15% for OC and < 10% for  
134 EC. More information of the OC and EC measurement procedures may be found in Cao et al. (2003).  
135 Thirteen elements were determined by energy-dispersive X-ray fluorescence (ED-XRF) spectrometry  
136 (Epsilon 5 ED-XRF, PANalytical B.V., Netherlands), and these elements include Al, Si, K, Ca, Ti, Cr,  
137 Mn, Fe, Cu, Zn, As, Br, and Pb. The analytical accuracy for ED-XRF measurements was determined with  
138 a NIST Standard Reference Material 2783 (National Institute of Standards and Technology, Gaithersburg,  
139 MD, USA). A more detailed description of the ED-XRF methods may be found in Xu et al. (2012).

#### 140 **2.2.2 Online measurements**

141 The aerosol optical properties were determined using a Photoacoustic Extinctionmeter (PAX, Droplet  
142 Measurement Technologies, Boulder, CO, USA) at a wavelength of 532 nm. The PAX measured light  
143 scattering ( $b_{\text{scat}}$ ) and absorption ( $b_{\text{abs}}$ ) coefficients (in  $\text{Mm}^{-1}$ ) simultaneously using a built-in wide-angle  
144 integrating reciprocal nephelometer and a photoacoustic technique, respectively. Before and during the  
145 sampling, the PAX  $b_{\text{scat}}$  and  $b_{\text{abs}}$  were calibrated using ammonium sulfate and fullerene soot particles,  
146 respectively, which were generated with an atomizer (Model 9302, TSI Inc., Shoreview, MN, USA).  
147 Detailed calibration procedures have been described in Wang et al. (2018a; 2018b). For this study, the  
148 PAX was fitted with a  $\text{PM}_{2.5}$  cutoff inlet, and the sampled particles were dried by a Nafion® dryer (MD-  
149 700-24S-1; Perma Pure, LLC., Lakewood, NJ, USA). The time resolution of the data logger was set to 1  
150 minute.

151 One-minute average mixing ratios of  $\text{NO}_x$  ( $\text{NO} + \text{NO}_2$ ),  $\text{O}_3$ , and  $\text{SO}_2$  were measured using a Model 42i  
152 gas-phase chemiluminescence  $\text{NO}_x$  analyzer (Thermo Fisher Scientific, Inc., Waltham, MA, USA), a  
153 Model 49i photometric ozone analyzer (Thermo Fisher Scientific, Inc.), and a Model 43i pulsed UV  
154 fluorescence analyzer (Thermo Fisher Scientific, Inc.), respectively. Standard reference  $\text{NO}$ ,  $\text{O}_3$ , and  $\text{SO}_2$   
155 gases were used to calibrate the  $\text{NO}_x$ ,  $\text{O}_3$ , and  $\text{SO}_2$  analyzers, respectively, before and during the campaign.  
156 All the online data were averaged to 24 h and matched to the duration of the filter sampling.

### 157 2.2.3 Complementary data

158 Wind speed (WS) and relative humidity (RH) were measured with the use of an automatic weather station  
159 installed at the Xianghe Atmospheric Observatory. Surface weather charts for East Asia were obtained  
160 from the Korea Meteorological Administration. The three-day backward in time trajectories and mixed  
161 layer heights (MLHs) were calculated using the Hybrid Single-Particle Lagrangian Integrated Trajectory  
162 (HYSPLIT) model (Draxler and Rolph, 2003), which was developed by the National Oceanic and  
163 Atmospheric Administration (NOAA). The aerosol optical depth (AOD) was measured using a  
164 sunphotometer (Cimel Electronique, Paris, France), and those data were obtained from the Aerosol  
165 Robotic Network data archive (<http://aeronet.gsfc.nasa.gov>). Fire counts were obtained from the  
166 Moderate Resolution Imaging Spectroradiometer (MODIS) instruments on the Aqua and Terra satellites  
167 (<https://firms.modaps.eosdis.nasa.gov/map>).

## 168 2.3 Data analysis methods

### 169 2.3.1 Chemical mass closure

170 The chemically reconstructed PM<sub>2.5</sub> mass was calculated as the sum of OM, EC, SO<sub>4</sub><sup>2-</sup>, NO<sub>3</sub><sup>-</sup>, NH<sub>4</sub><sup>+</sup>, Cl<sup>-</sup>,  
171 fine soil, and trace elements. A factor of 1.6 was used to convert OC to OM (OM = 1.6 × OC) to account  
172 for those unmeasured atoms in organic materials based on the results of Xu et al. (2015). The mass  
173 concentration of fine soil was calculated by summing the masses of Al, Si, K, Ca, Ti, Mn, and Fe oxides  
174 using the following equation (Cheung et al., 2011):

$$175 \text{ [Fine soil]} = [\text{Al}_2\text{O}_3] + [\text{SiO}_2] + [\text{K}_2\text{O}] + [\text{CaO}] + [\text{TiO}_2] + [\text{MnO}_2] + [\text{Fe}_2\text{O}_3]$$
$$176 = 1.89 \times [\text{Al}] + 2.14 \times [\text{Si}] + 1.21 \times [\text{K}] + 1.4 \times [\text{Ca}] + 1.67 \times [\text{Ti}] + 1.58 \times [\text{Mn}] + 1.43 \times [\text{Fe}] \quad (1)$$

177 The mass concentration of trace elements was calculated as the sum of measured elements that were not  
178 used in the calculation of fine soil:

$$179 \text{ [Trace elements]} = [\text{Cr}] + [\text{Cu}] + [\text{Zn}] + [\text{As}] + [\text{Br}] + [\text{Pb}] \quad (2)$$

180 As shown in Figure S1, the reconstructed PM<sub>2.5</sub> mass was strongly correlated ( $r = 0.98$ ) with the  
181 gravimetrically determined values, and this attests to the validity of the chemical reconstruction method.  
182 The slope of 0.86 indicates that our measured chemical species accounted for most of the PM<sub>2.5</sub> mass.  
183 The difference between the reconstructed and measured PM<sub>2.5</sub> mass was defined as “others”.

### 184 2.3.2 Receptor model source apportionment

185 Positive matrix factorization (PMF) has been widely used in source apportionment studies in the past two  
186 decades (e.g., Cao et al., 2012; Xiao et al., 2014; Tao et al., 2014; Huang et al., 2017). The principles of  
187 PMF are described in detail elsewhere (Paatero and Tapper, 2006). Briefly, PMF is a bilinear factor model  
188 that decomposes an initial chemically-speciated dataset into a factor contribution matrix  $G_{ik}$  ( $i \times k$   
189 dimensions) and a factor profile matrix  $F_{kj}$  ( $k \times j$  dimensions) and then iteratively minimizes the object  
190 function  $Q$ :

$$191 X_{ij} = \sum_{k=1}^p G_{ik}F_{kj} + E_{ij} \quad (3)$$

$$192 Q = \sum_{i=1}^m \sum_{j=1}^n \left( \frac{E_{ij}}{\sigma_{ij}} \right)^2 \quad (4)$$

193 where  $X_{ij}$  is the concentration of the  $j$ th species measured in the  $i$ th sample;  $E_{ij}$  is the model residual; and  
194  $\sigma_{ij}$  represents the uncertainty.

195 In this study, the PMF Model version 5.0 (PMF 5.0) from US Environmental Protection Agency (EPA)  
196 (Norris et al., 2014) was employed to identify the  $PM_{2.5}$  sources. Four to nine factors were extracted to  
197 determine the optimal number of factors with random starting points. When the values of scaled residuals  
198 for all chemical species varied between -3 and +3 and a small  $Q_{\text{true}}/Q_{\text{expect}}$  was obtained, the base run was  
199 considered to be stable. Further, bootstrap analysis (BS), displacement analysis (DISP), and bootstrap-  
200 displacement analysis (BS-DISP) were applied to assess the variability and stability of the results. A more  
201 detailed description of the methods for the determination of uncertainties in PMF solutions can be found  
202 in Norris et al. (2014).

### 203 2.3.3 Regional chemical dynamical model

204 The Weather Research and Forecasting model coupled to chemistry model (WRF-Chem) is a 3-D online-  
205 coupled meteorology and chemistry model, and it was used to simulate the formation processes that led  
206 to high  $PM_{2.5}$  loadings after the NCCPC. The WRF-Chem uses meteorological information, including  
207 clouds, boundary layer, temperature, and winds; pollutant emissions; chemical transformation; transport  
208 (e.g., advection, convection, and diffusion); photolysis and radiation; dry and wet deposition; and aerosol  
209 interactions. A detailed description of the WRF-Chem model may be found in Li et al. (2011a; 2011b;  
210 2012). A grid of  $280 \times 160$  cells covering China with a horizontal resolution of  $0.25^\circ$  was used for the  
211 simulation, which also included twenty-eight vertical layers from the Earth's surface up to 50 hPa. Seven  
212 layers below 1 km were used to ensure a high vertical resolution near ground-level. The meteorological

213 initial and boundary conditions were retrieved from the National Centers for Environmental Prediction  
 214 (NCEP) reanalysis dataset, and the chemical initial and boundary conditions were obtained from the 6 h  
 215 output of the Model for Ozone and Related chemical Tracers (MOZART, Emmons et al., 2010).

216 In this study, the mean bias (MB), root mean square error (RMSE), and index of agreement (IOA) were  
 217 used to evaluate the performance of WRF-Chem simulation. The IOA is representative of the relative  
 218 difference between the predicted and measured values, and it varies from 0 to 1, with 1 indicating perfect  
 219 performance of the model prediction. These parameters were calculated using the following equations (Li  
 220 et al., 2011a):

$$221 \quad MB = \frac{1}{N} \sum_{i=1}^N (P_i - O_i) \quad (5)$$

$$222 \quad RMSE = \left[ \frac{1}{N} \sum_{i=1}^N (P_i - O_i)^2 \right]^{\frac{1}{2}} \quad (6)$$

$$223 \quad IOA = 1 - \frac{\sum_{i=1}^N (P_i - O_i)^2}{\sum_{i=1}^N (|P_i - P_{ave}| + |O_i - O_{ave}|)^2} \quad (7)$$

224 where  $P_i$  and  $P_{ave}$  represent each predicted  $PM_{2.5}$  mass concentration and the average value, respectively;  
 225  $O_i$  and  $O_{ave}$  are the observed  $PM_{2.5}$  mass concentrations and the average value, respectively; and  $N$  is  
 226 representative of the total number of predictions used for comparison.

### 227 2.3.4 Calculations of chemical $b_{scat}$ and $b_{abs}$

228 To determine the contributions of individual  $PM_{2.5}$  chemical species to particles' optical properties,  $b_{scat}$   
 229 and  $b_{abs}$  were reconstructed based on the major chemical composition of the  $PM_{2.5}$  using the revised  
 230 IMPROVE equations as follows (Pitchford et al., 2007):

$$231 \quad b_{scat} \approx 2.2 \times f_S(RH) \times [(NH_4)_2SO_4]_{small} + 4.8 \times f_L(RH) \times [(NH_4)_2SO_4]_{large} + 2.4 \times f_S(RH) \times \\ 232 \quad [NH_4NO_3]_{small} + 5.1 \times f_L(RH) \times [NH_4NO_3]_{large} + 2.8 \times [OM]_{small} + 6.1 \times [OM]_{large} + 1 \times \\ 233 \quad [Fine\ soil] \quad (8)$$

$$234 \quad [X]_{large} = \frac{[X]^2}{20 \mu g m^{-3}}, \text{ for } [X] < 20 \mu g m^{-3} \quad (9)$$

$$235 \quad [X]_{large} = [X], \text{ for } [X] \geq 20 \mu g m^{-3} \quad (10)$$

$$236 \quad [X]_{small} = [X] - [X]_{large} \quad (11)$$

237 where the mass concentrations of ammonium sulfate ( $[(NH_4)_2SO_4]$ ) and ammonium nitrate ( $[NH_4NO_3]$ )  
 238 were estimated by multiplying the concentrations of  $SO_4^{2-}$  and  $NO_3^-$  by factors of 1.375 and 1.29,

239 respectively (Tao et al., 2014);  $f(\text{RH})$  is the water growth for the small (S) and large (L) modes of  
240  $(\text{NH}_4)_2\text{SO}_4$  and  $\text{NH}_4\text{NO}_3$  in  $\text{PM}_{2.5}$ ; and  $[X]$  represents the  $\text{PM}_{2.5}$  composition as used in Eq. (8). This  
241 analysis is based on the assumption that the particles were externally mixed. More detailed information  
242 concerning the IMPROVE algorithms may be found in Pitchford et al. (2007).

243 A second assumption for this part of the study was that there was negligible absorption by brown carbon  
244 in the visible region (Yang et al., 2009), and on this basis, the  $b_{\text{abs}}$  can be determined from the EC mass  
245 concentration using linear regression (Eq. 12). As shown in Figure S2, the derived slope (a) and intercept  
246 (b) for the regression model were  $10.8 \text{ m}^2 \text{ g}^{-1}$  and  $-4.7$ , respectively.

$$247 \quad b_{\text{abs}} = a \times [\text{EC}] + b \quad (12)$$

### 248 2.3.5 DRF calculations

249 The Tropospheric Ultraviolet and Visible (TUV) radiation model developed by the National Center for  
250 Atmospheric Research was used to estimate the aerosol DRF for 180–730 nm at the Earth's surface. A  
251 detailed description of the model may be found in Madronich (1993). Aerosol DRF is mainly controlled  
252 by the aerosol column burden and chemical composition, and important properties include the AOD,  
253 aerosol absorption optical depth (AAOD), and single-scattering albedo ( $\text{SSA} = (\text{AOD} - \text{AAOD}) / \text{AOD}$ ).  
254 Based on an established relationship between the AODs measured with sunphotometer and the light  
255 extinction coefficients ( $b_{\text{ext}} = b_{\text{scat}} + b_{\text{abs}}$ ) observed with PAXs, an effective height can be retrieved which  
256 makes it possible to convert the IMPROVE-based chemical  $b_{\text{ext}}$  values into the AODs or AAODs caused  
257 by the  $\text{PM}_{2.5}$ . There are hygroscopic effects to consider, and therefore, the dry  $b_{\text{ext}}$  values measured here  
258 were modified to the wet  $b_{\text{ext}}$  based on the water-growth function of particles described in Malm et al.  
259 (2003). We note that the estimated chemical AODs were based on the assumption that the aerosols were  
260 distributed homogeneously throughout an effective height.

261 Finally, the calculated chemical AOD and SSA for different  $\text{PM}_{2.5}$  composition scenarios were used in  
262 the TUV model to obtain shortwave radiative fluxes. Values for the surface albedo, another factor that  
263 influences DRF, were obtained from the MOD43B3 product measured with the Moderate Resolution  
264 Imaging Spectroradiometer (<https://modis-atmos.gsfc.nasa.gov/ALBEDO/index.html>). The solar  
265 component in the TUV model was calculated using the  $\delta$ -Eddington approximation, and the vertical  
266 profile of  $b_{\text{ext}}$  used in the model was described in Palancar and Toselli (2004). The aerosol DRF is defined  
267 as the difference between the net shortwave radiative flux with and without aerosol as follows:

$$268 \quad \text{DRF}_{\text{surface}} = \text{Flux (net)}_{\text{with aerosol, surface}} - \text{Flux (net)}_{\text{without aerosol, surface}} \quad (13)$$

## 269 3 Results and discussion

### 270 3.1 Effectiveness of the control measures on reducing PM<sub>2.5</sub>

271 We divided the study period into two phases based on the dates that the pollution control measures were  
272 put into effect (1) the NCCPC-control period from 12 to 24 October and (2) non-control period from 25  
273 October to 4 November. Temporal variations in the PM<sub>2.5</sub> mass concentrations and those of the major  
274 aerosol components during these two phases are shown in Figure 2, and a statistical summary of those  
275 data is presented in Table 1. During the NCCPC-control period, the PM<sub>2.5</sub> mass concentrations remained  
276 consistently low relative to the NAAQS II (75  $\mu\text{g m}^{-3}$ ), generally  $< 75 \mu\text{g m}^{-3}$ . In contrast, higher fine  
277 particle loadings (PM<sub>2.5</sub>  $> 75 \mu\text{g m}^{-3}$ ) frequently were observed during the non-control period. On average,  
278 the mass concentration of PM<sub>2.5</sub> during the NCCPC-control period was  $57.9 \pm 9.8 \mu\text{g m}^{-3}$ , which is lower  
279 by 31.2% compared with the non-control period ( $84.1 \pm 38.8 \mu\text{g m}^{-3}$ ). Meanwhile, the PM<sub>2.5</sub> mass  
280 concentrations obtained from the China Environmental Monitoring Center also showed a decreasing trend  
281 over most of the BTH region during the NCCPC-control period (see Figure S3). Compared with previous  
282 events when pollution control measures were implemented in Beijing and surrounding areas, the percent  
283 decrease in PM<sub>2.5</sub> found for the present study falls within the lower limit of the 30–50% reduction for  
284 Olympic Games (Wang et al., 2009; Li et al., 2013), but it is less than the range of 40–60% for the APEC  
285 (Tang et al., 2015; Tao et al., 2016; J. Wang et al., 2017) or the range of 60–70% for the VDP (Han et al.,  
286 2016; Liang et al., 2017; Lin et al., 2017).

287 As shown in Figure 2 (right panel), the chemical mass closure calculations for PM<sub>2.5</sub> showed that on  
288 average OM was the largest contributor (30.4%) to PM<sub>2.5</sub> mass during the non-control period, followed  
289 by NO<sub>3</sub><sup>-</sup> (16.7%), fine soil (11.2%), and EC (7.6%). In contrast, OM (24.3%) and NO<sub>3</sub><sup>-</sup> (22.9%) dominated  
290 the PM<sub>2.5</sub> mass during the NCCPC-control period, followed by SO<sub>4</sub><sup>2-</sup> (9.8%), NH<sub>4</sub><sup>+</sup> (9.1%), and EC (7.9%).  
291 The OM mass concentration was decreased largely by 43.1% from 24.6  $\mu\text{g m}^{-3}$  during the non-control  
292 period to 14.0  $\mu\text{g m}^{-3}$  during the NCCPC-control period. For secondary water-soluble inorganic ions, the  
293 average mass concentrations of NO<sub>3</sub><sup>-</sup> (13.4  $\mu\text{g m}^{-3}$  versus 16.9  $\mu\text{g m}^{-3}$ ) and NH<sub>4</sub><sup>+</sup> (5.4 versus 6.8  $\mu\text{g m}^{-3}$ )  
294 were lower by 20.7% and 20.6% during the NCCPC-control period, respectively. However, SO<sub>4</sub><sup>2-</sup>  
295 exhibited similar loadings during the NCCPC-control (5.8  $\mu\text{g m}^{-3}$ ) and non-control (5.3  $\mu\text{g m}^{-3}$ ) periods.  
296 This is consistent with the small differences in SO<sub>2</sub> concentrations for the NCCPC-control (8.5  $\mu\text{g m}^{-3}$ ,  
297 Figure S4) versus the non-control (12.4  $\mu\text{g m}^{-3}$ , Figure S4) periods. Indeed, the low SO<sub>2</sub> concentrations  
298 may not have provided sufficient gaseous precursor to form substantial amounts of sulfate. The loadings  
299 of EC, Cl<sup>-</sup>, and fine soil were lower by 25.0, 44.8, and 40.8%, respectively, when the controls were in

300 place. The variations in reductions for specific aerosol components imply differences in the effectiveness  
301 of the emission controls on the chemical species, but as discussed below, meteorological conditions  
302 probably had an influence on the loadings, too.

303 As shown in Figure S4, both WSs ( $0.7 \pm 0.3$  versus  $1.3 \pm 0.8 \text{ m s}^{-1}$ ) and MLHs ( $304.3 \pm 60.6$  versus  $373.7$   
304  $\pm 217.9 \text{ m}$ ) were lower for the NCCPC-control period compared with the non-control period. This  
305 indicates that horizontal and vertical dispersion were weaker during the NCCPC-control period than in  
306 the non-control period. More to the point, this shows that one needs to consider the effects of WS and  
307 MLH to fully evaluate the effectiveness of the pollution control measures. A simple and effective way to  
308 do this is to compare the concentrations of air pollutants for the two periods when atmospheric conditions  
309 were stable (Wang et al., 2015; Liang et al., 2017).

310 We first evaluated atmospheric stability based on relationships between  $\text{PM}_{2.5}$  mass concentrations and  
311 WS and MLH. As shown in Figure 3, the  $\text{PM}_{2.5}$  mass concentrations exhibited a power function  
312 relationship with WS ( $r = -0.65$ ) and MLH ( $r = 0.77$ ). The approach used to determine stable conditions  
313 was to find the WS and MLH values that were less than the inflection points in the  $\text{PM}_{2.5}$  loadings; that  
314 is, where the slopes in the loadings changed from large to relatively small values. As there are no true  
315 inflection points for the power functions, we used piecewise functions to represent them. As shown in  
316 Figure 3, the intersections of two linear regressions can be used to represent the inflection points of the  
317 influences of meteorological conditions on  $\text{PM}_{2.5}$  mass. Using these criteria, days with  $\text{WS} < 0.4 \text{ m s}^{-1}$   
318 and  $\text{MLH} < 274 \text{ m}$  were subjectively considered to have stable atmospheric conditions.

319 There were two days for the NCCPC-control period and three days for the non-control period that satisfied  
320 the stability criteria. The surface charts (Figure S5) show that the weather conditions for those selected  
321 stable atmosphere days during the NCCPC-control and non-control periods were mainly controlled by  
322 uniform pressure fields and weak low-pressure systems, respectively, and those conditions led to weak or  
323 calm surface winds. Due to the lower WS ( $0.2$  versus  $0.3 \text{ m s}^{-1}$ ) and MLH ( $213$  versus  $244 \text{ m}$ ) during the  
324 NCCPC-control period relative to the non-control period, the horizontal and vertical dispersion for the  
325 stable atmospheric days were slightly weaker during the NCCPC-control period. As shown in Table 1,  
326 the percent differences for  $\text{PM}_{2.5}$  (43.4%),  $\text{NO}_3^-$  (25.9%), OM (68.1%), EC (40.0%), and fine soil (58.7%)  
327 were larger for the days with stable atmospheric conditions compared with those for all days. These results  
328 are a further indication that the control measures were effective in reducing pollution, but meteorology  
329 also influenced the aerosol pollution.

### 330 3.2 Estimates of source contributions

331 The mass concentrations of water-soluble inorganic ions ( $\text{SO}_4^{2-}$ ,  $\text{NO}_3^-$ ,  $\text{NH}_4^+$ ,  $\text{K}^+$ , and  $\text{Cl}^-$ ), carbonaceous  
332 (OC and EC), and elements (Al, Si, Ca, Ti, Cr, Mn, Fe, Cu, Zn, As, Br, and Pb) were used as data inputs  
333 for the PMF 5.0 model. Through comparisons between the PMF profiles and reference profiles from  
334 previous studies, the presumptive sources for the aerosol were identified as (i) coal combustion, (ii)  
335 traffic-related emissions, (iii) secondary source, (iv) biomass burning, (v) industrial processes, and (vi)  
336 mineral dust. As shown in Figure S6, the PMF modelled  $\text{PM}_{2.5}$  mass concentrations were strongly  
337 correlated with the observed values ( $r = 0.98$ , slope = 0.94), and the model-calculated concentrations for  
338 each chemical species exhibited good linearity and correlations with the measured values ( $r = 0.68\text{--}0.99$ )  
339 (Table S1). These results show that the six identified sources were physically interpretable and accounted  
340 for much of the variability in the data.

341 Figure 4 presents the source profiles and the average contribution of each source to  $\text{PM}_{2.5}$  mass during  
342 the NCCPC-control and non-control periods. The first source factor was identified as coal burning  
343 emissions because it was enriched with As (38.8%), Pb (32.9%), and Fe (30.3%) and had moderate  
344 loadings of Mn (26.2%), Zn (23.8%), Si (23.1%), and Ca (22.8%) (Figure 4a). Of these elements, As is a  
345 well-known tracer for coal burning (Hsu et al., 2009; Y. Chen et al., 2017); Pb, Fe, Mn, and Zn (Xu et al.,  
346 2012; Men et al., 2018) are enriched in particles generated by this source; and Ca and Si can be  
347 components of coal fly ash (Pipal et al., 2011). There was no significant difference in  $\text{PM}_{2.5}$  loadings  
348 contributed by this source between the NCCPC-control ( $8.5 \mu\text{g m}^{-3}$ ) and non-control ( $7.8 \mu\text{g m}^{-3}$ ) periods.  
349 This may be because coal burning is mainly used for domestic purposes, especially heating, and the  
350 control measures did not include this sector. The contribution of coal burning to  $\text{PM}_{2.5}$  mass in our  
351 October/November study was lower than its contribution in the BTH region in winter ( $\sim 20\text{--}60 \mu\text{g m}^{-3}$ )  
352 (Huang et al., 2017), and that can be explained by the increased domestic usage of coal for heating  
353 activities during the colder winter season.

354 The second source factor was linked to traffic-related emissions, and it was characterized by strong  
355 loadings of EC (42.1%) and Cu (40.7%) and moderate contributions of OC (29.1%), Zn (27.1%), and Br  
356 (22.2%). Previous studies have indicated that carbonaceous aerosols are components of gasoline and  
357 diesel engine exhaust (Cao et al., 2005), and therefore, EC and OC have been used as indicators for motor  
358 vehicle emissions (Chalbot et al., 2013; Khan et al., 2016a), and Br, too, may be emitted from internal  
359 combustion engines (Bukowiecki et al., 2005). Aerosol Cu and Zn are derived from other types of vehicle  
360 emissions, including those associated with lubricant and oil, brake linings, metal brake wear, and tires

删除的内容: particle formation

362 (Lin et al., 2015). Furthermore, the mass concentration of PM<sub>2.5</sub> from this source was strongly correlated  
363 ( $r = 0.72$ ) with vehicle-related NO<sub>x</sub> concentrations (Figure S7), which further suggests the validity of this  
364 PMF-resolved source. Traffic-related emissions showed similar percent contributions to PM<sub>2.5</sub> mass  
365 during the NCCPC-control (14.8%) and non-control (15.4%) periods (Figure 4c), but the mass  
366 concentration was 38% lower for the NCCPC-control period ( $8.9 \mu\text{g m}^{-3}$ ) than the non-control period  
367 ( $14.4 \mu\text{g m}^{-3}$ ). This shows that the reduction in motor vehicle activity during the control period led to  
368 better air quality.

369 The third source factor was a clear signal of secondary particle formation because it was dominated by  
370 high loadings of SO<sub>4</sub><sup>2-</sup> (45.4%), NO<sub>3</sub><sup>-</sup> (43.4%), and NH<sub>4</sub><sup>+</sup> (47.0%) (Zhang et al., 2013; Amil et al., 2016).  
371 **Thus, this factor was assigned to the secondary source.** Moreover, moderate loadings of As (30.5%), Pb  
372 (27.4%), Cr (31.4%), Cu (30.7%), and EC (30.8%) also were assigned to this factor, suggesting influences  
373 from coal burning and vehicle exhaust emissions. Although the concentrations of gaseous precursors,  
374 especially SO<sub>2</sub> and NO<sub>x</sub>, were lower during the NCCPC-control period (Figure S4), the average mass  
375 contribution of secondary PM<sub>2.5</sub> was larger when the controls were in effect (22.5 versus  $18.3 \mu\text{g m}^{-3}$ );  
376 indeed, this source was the largest contributing factor (37.3% of PM<sub>2.5</sub> mass) during the NCCPC-control  
377 period. We note that the higher RH (84%) during the NCCPC-control period compared with the non-  
378 control period (69%) may have promoted the formation of the secondary inorganic aerosols through  
379 aqueous reactions (Sun et al., 2014).

380 The fourth source factor, identified as emissions from biomass burning, was characterized by the high  
381 loadings of K<sup>+</sup> (59.5%) and moderate loadings of Cl<sup>-</sup> (33.3%), OC (28.5%), NO<sub>3</sub><sup>-</sup> (37.1%), SO<sub>4</sub><sup>2-</sup> (21.1%),  
382 and NH<sub>4</sub><sup>+</sup> (39.6%). Soluble K<sup>+</sup> is an established tracer for biomass burning (Zhang et al., 2013; Wang et  
383 al., 2016b), and Cl<sup>-</sup> and OC also are emitted during biomass burning (Tao et al., 2014; Huang et al., 2017).  
384 Previous studies have shown that SO<sub>2</sub> and NO<sub>2</sub> can be converted into sulfate and nitrate on KCl particles  
385 during the transport of biomass-burning emissions (Du et al., 2011). Therefore, the abundant NO<sub>3</sub><sup>-</sup>, SO<sub>4</sub><sup>2-</sup>,  
386 and NH<sub>4</sub><sup>+</sup> associated with this factor may be indicative of aged biomass-burning particles. As shown in  
387 Figure 4c, biomass burning contributed substantially to PM<sub>2.5</sub> mass during both the NCCPC (21.6%) and  
388 non-control periods (27.3%). This is to be expected because Hebei Province is a major corn and wheat  
389 producing area, and the residues of these crops commonly are used for residential cooking and heating or  
390 burned in the fields (J. Chen et al., 2017). The mass concentrations of PM<sub>2.5</sub> from this source were lower  
391 during the NCCPC ( $13.0 \mu\text{g m}^{-3}$ ) than in the non-control period ( $25.7 \mu\text{g m}^{-3}$ ), and this indicates the  
392 effectiveness of the control policy that forbade the open space biomass-burning during the NCCPC. As

393 the control measures did not include prohibitions on the household use of biofuels, substantial  
394 contributions of biomass burning were still evident during the NCCPC-control period.

395 The fifth source factor was identified as emissions from industrial processes because it had high loadings  
396 of Zn (41.3%), Br (38.0%), Pb (19.9%), As (19.2%), Cu (17.5%), and Mn (19.1%) (Q. Q. Wang et al.,  
397 2017; Sammaritano et al., 2018). This source contributed  $3.6 \mu\text{g m}^{-3}$  to  $\text{PM}_{2.5}$  mass during the NCCPC-  
398 control period, which was lower than the non-control period ( $16.2 \mu\text{g m}^{-3}$ ) by 78%, and its percent  
399 contribution to  $\text{PM}_{2.5}$  mass also increased correspondingly from 6.0 to 17.2% after the controls were  
400 removed. The results showed that restrictions on industrial activities during the NCCPC-control period  
401 led to improvements in air quality. Iron and steel production are among the most important industries in  
402 BTH region, and the iron and steel production there accounted for 28.8% of the total for China in 2016  
403 (NBS, 2017). The sintering process in iron and steel industries produce large amounts of heavy metal  
404 pollutants including Zn, Pb, and Mn (Duan and Tan, 2013). Hence, the iron and steel industries in the  
405 BTH region were probable sources for these metals during the non-control period.

406 The sixth source factor was obviously mineral dust because it had high loadings of Al (55.9%), Si (55.7%),  
407 Ca (52.6%), and Ti (36.7%) (Zhang et al., 2013; Tao et al., 2014; Kuang et al., 2015). This factor  
408 contributed  $3.8 \mu\text{g m}^{-3}$  (6.3% of  $\text{PM}_{2.5}$  mass) during the NCCPC-control period and  $11.5 \mu\text{g m}^{-3}$  (12.3%)  
409 to  $\text{PM}_{2.5}$  mass in the non-control period. Possible sources for the mineral dust include (i) natural dust,  
410 which contains crustal Al, Si, and Ti (Milando et al., 2016), (ii) construction dust, which includes Ca (Liu  
411 et al., 2017), and (iii) road dust, which is characterized by traffic-related species, such as Cu, Zn, Br, and  
412 EC (Khan et al., 2016b; Zong et al., 2016). Here, the mineral dust factor did not contain any notable  
413 contributions from the traffic-related species. Thus, this factor can be explained by the natural and  
414 construction dusts. As shown in Figure S8, WS was positively correlated ( $r = 0.75$ ) with the  $\text{PM}_{2.5}$  mass  
415 from mineral dust. To reduce the effects of wind speed on crustal dust resuspension, we compared the  
416 days with low winds ( $< 1 \text{ m s}^{-1}$ ) during the sampling periods, and only three sampling days were excluded  
417 from the analysis. This comparison showed that the mass concentration of  $\text{PM}_{2.5}$  from mineral dust was  
418 60.0% lower in the NCCPC-control period ( $3.8 \mu\text{g m}^{-3}$ ) compared with the non-control period ( $9.5 \mu\text{g m}^{-3}$ ).  
419 This was a strong indication that restrictions on construction activities during the NCCPC-period were  
420 effective in reducing the mineral dust component of  $\text{PM}_{2.5}$ , but as noted above, this was not a large  
421 component of the  $\text{PM}_{2.5}$  mass.

删除的内容: is

删除的内容: is

### 424 3.3 Pollution episodes after the NCCPC-control period

425 As shown in Figure 2 (left panel), two pollution episodes occurred after the NCCPC-control period (PE1:  
426 25–27 October and PE2: 31 October–1 November); the average PM<sub>2.5</sub> mass concentrations in PE1 and  
427 PE2 were 117.5 and 124.5 μg m<sup>-3</sup>, respectively. For PE1, secondary ~~source was~~ the dominant contributor  
428 to the fine particle population, accounting for 54.6% of PM<sub>2.5</sub> mass (Figure 5a), and the secondary species  
429 that showed the largest contribution to PM<sub>2.5</sub> mass was NO<sub>3</sub><sup>-</sup> (26.8%) (Figure 5b). The mass concentration  
430 of NO<sub>3</sub><sup>-</sup> increased from < 10 μg m<sup>-3</sup> before PE1 to > 25 μg m<sup>-3</sup> during the episode (Figure 2). Molar ratios  
431 of NO<sub>3</sub><sup>-</sup> to NO<sub>2</sub> (NOR = n-NO<sub>3</sub><sup>-</sup>/(n-NO<sub>2</sub> + n-NO<sub>3</sub><sup>-</sup>)) were calculated to investigate nitrogen partitioning  
432 between the particulate and gas phases (Zhang et al., 2011). As shown in Figure 6a, the mass concentration  
433 of PM<sub>2.5</sub> increased with NOR (r = 0.65) throughout the entire campaign, which indicates that nitrate  
434 formation was involved in the high PM<sub>2.5</sub> loadings. The NORs ranged from 0.32 to 0.71 during the PE1,  
435 and those values were significantly different (*t*-test, *p* < 0.01) from the ratios before (0.23–0.29) or after  
436 PE1 (0.03–0.10), thus reflecting stronger nitrate formation during the pollution period. Furthermore, NOR  
437 exhibited an exponential increase with RH (r = 0.80, Figure 6b), and the higher RHs (91–93%) during the  
438 PE1 may have led to greater aqueous nitrate production relative to the periods before (80–86%) or after  
439 (33–57%) the first pollution episode.

440 The second largest contributor to PM<sub>2.5</sub> mass during PE1 was OM, which accounted for 22.9% of the fine  
441 aerosol mass. A widely used EC-tracer method (Lim and Turpin, 2002) was used to estimate the primary  
442 and secondary OA (POA and SOA). For this, the lowest 10% percentile of the measured OC/EC ratios  
443 was used as a measure of the primary OC/EC ratio (Zheng et al., 2015). The estimated mass  
444 concentrations of POA and SOA were 17.2 and 9.7 μg m<sup>-3</sup> during the PE1, which amounted to 63.9 and  
445 36.1% of the OM mass, respectively.

446 Photochemical oxidation and aqueous reactions are two of the major mechanisms that lead to the  
447 formation SOA (Hallquist et al., 2009), and we evaluated the roles of these chemical reactions by  
448 investigating trends in the EC-scaled concentrations of SOA (SOA/EC). We note that normalizing the  
449 data in this way eliminates the impacts of different dilution/mixing conditions on the SOA loadings  
450 (Zheng et al., 2015). As shown in Figure 6c, the SOA/EC ratios increased (r = 0.65) with Ox (NO<sub>2</sub> + O<sub>3</sub>),  
451 which is a proxy for atmospheric aging caused by photochemical reactions (Canonaco et al., 2015), and  
452 the EC-scaled concentrations showed a weaker correlation with RH (r = -0.32) (Figure 6d). These results  
453 indicate that photochemical reactions rather than aqueous phase oxidation were the major pathways for

删除的内容: aerosols

删除的内容: w

删除的内容: ere

457 SOA formation. Thus, the small contribution of SOA to  $PM_{2.5}$  during the PE1 may have been due to low  
458 photochemical activity during that episode.

459 In contrast to the first pollution episode, OM (31.8%) was the most abundant  $PM_{2.5}$  species during PE2,  
460 and that was followed by  $NO_3^-$  (19.2%) (Figure 5b). The mass concentration of  $K^+$  increased substantially,  
461 from  $0.1 \mu\text{g m}^{-3}$  before PE2 to  $1.7 \mu\text{g m}^{-3}$  during the event, indicating a strengthening influence of  
462 biomass-burning emissions. Indeed, the results of PMF showed that biomass burning was the largest  
463 contributor to  $PM_{2.5}$  mass during the PE2, accounting for 36.0% of the total (Figure 5a). Furthermore, the  
464 72-h back trajectories showed that air masses sampled during the PE2 either originated from or passed  
465 over areas with fires in Inner Mongolia and Shanxi Province (see Figure 7), and this can explain the  
466 apparent impacts from biomass burning emission. Moreover, SOA contributed an estimated 47.7% of the  
467 OM mass, and that is a strong indication that secondary organics were a major component of the pollution.  
468 The mass concentration of SOA was  $19.0 \mu\text{g m}^{-3}$  during the PE2, and that was higher than in  $9.7 \mu\text{g m}^{-3}$   
469 during the PE1. As the oxidizing conditions—as indicated by  $O_x$ —were similar for both pollution  
470 episodes ( $78.0 \mu\text{g m}^{-3}$  in PE1 versus  $86.7 \mu\text{g m}^{-3}$  in PE2) (Figure S4), the larger SOA during the PE2 can  
471 best be explained by SOA that formed from gaseous biomass-burning emissions during transport.

### 472 3.4 Meteorological considerations

473 Previous studies have shown that meteorological conditions play an important role in the accumulation  
474 of pollution in the BTH region (Bei et al., 2017). Surface weather charts (Figure 8) were used to analyze  
475 the synoptic conditions during the two pollution episodes, and the WRF-Chem model was applied to  
476 simulate the formation of  $PM_{2.5}$  (Figure 9). As shown in Figure S9, the predicted  $PM_{2.5}$  and its major  
477 chemical components exhibited trends roughly similar to the observed values. The calculated MB and  
478 RMSE for  $PM_{2.5}$  were  $-6.8$  and  $32.8 \mu\text{g m}^{-3}$ , and the IOA was 0.75, indicating that the formation of  $PM_{2.5}$   
479 during the two pollution episodes was reasonably well captured by the WRF-Chem model even though  
480 the predicted average  $PM_{2.5}$  mass concentration was lower than the observed value. The most probable  
481 reason for this is that uncertainties associated with the complex meteorological fields can affect the  
482 transport, diffusion, and removal of air pollutants in the atmosphere (Bei et al., 2012). Additionally,  
483 discrepancies in the emission inventories for  $PM_{2.5}$  for different years may have contributed to the  
484 differences in modelled versus measured values.

485 On 22 October, that is, before PE1, a weak cold high-pressure system in Siberia moved southward (Figure  
486 8), and the BTH region was under the influence of a cold high-pressure system; conditions such as those  
487 tend to keep pollutants at low levels. After the passage of the low-pressure system, the BTH region was

488 under the control of a weak high-pressure system from 24 to 25 October, and that led to a convergence of  
489 southerly airflow in the BTH region. Those meteorological conditions were favourable for the gradual  
490 accumulation of pollutants (Figure 9). For example, as shown in Figure S4, the NO<sub>x</sub> concentrations  
491 increased from 71.6 μg m<sup>-3</sup> on 22 October to 147.6 μg m<sup>-3</sup> on 25 October, and that increase provided a  
492 supply of gaseous precursors that can explain the observed large loadings of aerosol nitrate.

493 On 28 October, the first day of PE1, cold air piled up in the BTH region, and the high-pressure system  
494 gradually strengthened. The weather in the BTH region at that time was characterized by cloudiness, high  
495 RH, and low surface WSs. Those conditions promoted the accumulation of pollutants (Figure 9), and the  
496 WRF-Chem simulation indicated that the BTH region contributed 73.6% of PM<sub>2.5</sub> mass during PE1. On  
497 29 October, the cold high-pressure system moved towards the south, and northerly winds increased. Those  
498 meteorological conditions presumably led to a dilution of the air pollutants, and as a result, lower PM<sub>2.5</sub>  
499 loadings were observed in the BTH region (Figure 9).

500 From 31 October–1 November (PE2), the BTH region was again dominated by a weak high-pressure  
501 system, and a convergence of northerly airflow was caused by the high-pressure system and a trailing  
502 low-pressure front. Local pollutants from the BTH region would have accumulated under those conditions,  
503 but as discussed above, the loadings of PM<sub>2.5</sub> also can be affected by the long-range transport processes.  
504 Indeed, the WRF-Chem simulation indicated that the BTH region contributed 46.9% to PM<sub>2.5</sub> mass,  
505 similar to the import of fine particles from other regions (53.1%). After 2 November, the cold high-  
506 pressure system began to move southward, the winds strengthened, and the air quality gradually improved.

### 507 **3.5 Impacts of PM<sub>2.5</sub> emission reduction on aerosol radiative effects**

508 The aerosol DRF refers to the change in the energy balance caused by the scattering and absorption of  
509 radiant energy by aerosols. As shown in Figure S10, the reconstructed chemical  $b_{\text{scat}}$  correlated strongly  
510 ( $r = 0.91$ ) with the observed  $b_{\text{scat}}$  values; the slope of the linear regression was 0.90. This result indicates  
511 that the IMPROVE-based method provided a good estimation of the chemical  $b_{\text{scat}}$ ; nonetheless, it is likely  
512 that more locally-measured mass scattering efficiencies for each chemical species could reduce the  
513 underestimates of measured values. Moreover, a significant ( $p < 0.01$ ) relationship between the measured  
514  $b_{\text{abs}}$  and EC mass (Figure S2) validates the use of EC mass loadings in Eq. 12 to estimate the chemical  
515  $b_{\text{abs}}$ . The contributions of each measured PM<sub>2.5</sub> component to the chemical  $b_{\text{ext}}$  were calculated based on  
516 Eq. 8, and on average, OM was the largest contributor (43.5%) to the chemical  $b_{\text{ext}}$  during the non-control  
517 period (Figure 10a), followed by NH<sub>4</sub>NO<sub>3</sub> (32.4%), EC (14.3%), (NH<sub>4</sub>)<sub>2</sub>SO<sub>4</sub> (7.6%), and fine soil (2.2%).  
518 In contrast, during the NCCPC-control period, NH<sub>4</sub>NO<sub>3</sub> was the largest contributor to the chemical  $b_{\text{ext}}$ ,

519 amounting to 36.7% of  $b_{\text{ext}}$ , and it was followed by OM (33.3%), EC (16.2%),  $(\text{NH}_4)_2\text{SO}_4$  (11.9%), and  
520 fine soil (1.9%). The contributions of the various  $\text{PM}_{2.5}$  components to  $b_{\text{ext}}$  were different compared with  
521 previous studies of the pollution controls for the Olympics and APEC. For example, Li et al. (2013)  
522 reported that  $(\text{NH}_4)_2\text{SO}_4$  (41%) had the largest contribution to  $b_{\text{ext}}$  during the Olympics, followed by  
523  $\text{NH}_4\text{NO}_3$  (23%), OM (17%), and EC (9%); Zhou et al. (2017) found that OM (49%) was the largest  
524 contributor to  $b_{\text{ext}}$  during the APEC summit, followed by  $\text{NH}_4\text{NO}_3$  (19%),  $(\text{NH}_4)_2\text{SO}_4$  (13%), and EC  
525 (12%). These differences may be attributed to variable efficiencies of the controls for the specific fine  
526 particle species and to variations in RH among studies, the latter of which can influence sulfate and nitrate  
527 formation.

528 As shown in Figure S11, the AODs measured with a sunphotometer were well correlated with the  $b_{\text{ext}}$   
529 under ambient conditions; the slope (effective height) of the regression was 708 m and  $r = 0.78$ . Based on  
530 the average effective height, the estimated chemical AOD ( $\text{AOD} = 708 \times b_{\text{ext}} \times 10^{-6}$ ) and SSA contributed  
531 by each major component in  $\text{PM}_{2.5}$  were entered into the TUV model to calculate the DRF at the Earth's  
532 surface. The estimated average DRF ranged from -33.2 to -3.4  $\text{W m}^{-2}$ , with an arithmetic mean  $\pm$  standard  
533 deviation of  $-16.5 \pm 6.7 \text{ W m}^{-2}$  for the campaign. The average DRF for our study is similar to the -13.7  
534  $\text{W m}^{-2}$  calculated for photosynthetically active radiation at Xianghe, China in autumn using the Santa  
535 Barbara DISORT Atmospheric Radiative Transfer model (SBDART) (Xia et al., 2007a). Further  
536 comparisons with previous estimates of DRFs in China at ultraviolet and visible wavelengths show that  
537 the average value from our study is similar to that at the rural site of Taihu (-17.8  $\text{W m}^{-2}$ , Xia et al., 2007b),  
538 but it was less negative than at the suburban or urban sites of Linan (-73.5  $\text{W m}^{-2}$ , Xu et al., 2003), Nanjing  
539 (-39.4  $\text{W m}^{-2}$ , Zhuang et al., 2014), or Xi'an (-100.5  $\text{W m}^{-2}$ , Wang et al., 2016b). The more negative DRF  
540 values correspond with high aerosol loadings during those studies.

541 The estimated average DRF during the NCCPC-control period was  $-14.0 \pm 3.0 \text{ W m}^{-2}$ , which was less  
542 negative than the value during the non-control period ( $-19.3 \pm 8.6 \text{ W m}^{-2}$ ) (Figure 10b), and this is  
543 consistent with lower  $\text{PM}_{2.5}$  mass loadings during the NCCPC-control period. Even though the DRF  
544 values were as high as -24.7 and -28.2  $\text{W m}^{-2}$  during PE1 and PE2, respectively, the percent reduction in  
545 DRF during the NCCPC-control period versus the non-control period (26.3%) was smaller than the value  
546 during the APEC-control study (61.3%, Zhou et al., 2017). Figure 10b also indicates that EC was  
547 responsible for the largest (most negative) DRF effects at the surface during the non-control period: the  
548 EC DRF value of -13.4  $\text{W m}^{-2}$  was followed by OM (-3.0  $\text{W m}^{-2}$ ),  $\text{NH}_4\text{NO}_3$  (-2.2  $\text{W m}^{-2}$ ),  $(\text{NH}_4)_2\text{SO}_4$  (-  
549 0.5  $\text{W m}^{-2}$ ), and fine soil (-0.15  $\text{W m}^{-2}$ ). The high EC DRF may have been due in part to EC particles

internally mixed with other materials because mixing can amplify light absorption and thereby increase DRF. The lower aerosol loadings during the NCCPC-control period can explain why the DRF values for EC,  $\text{NH}_4\text{NO}_3$ , OM, and fine soil in the uncontrolled period were smaller in magnitude -10.1, -1.7, -1.6, and  $-0.09 \text{ W m}^{-2}$ , respectively, than in the non-control period; these were equivalent to decreases of 24.6, 22.7, 46.7, and 40.0%. These results suggest that the short-term mitigation measures implemented during the NCCPC reduced the cooling effects of  $\text{PM}_{2.5}$  at the surface in Beijing.

#### 4 Conclusions

We investigated the effects of pollution controls put in place during the 19th NCCPC on the chemical composition of  $\text{PM}_{2.5}$  and aerosol radiative effects at the Earth's surface. The average mass concentration of  $\text{PM}_{2.5}$  during the NCCPC-control period was  $57.9 \pm 9.8 \mu\text{g m}^{-3}$ , which was 31.2% lower relative to the non-control period ( $84.1 \pm 38.8 \mu\text{g m}^{-3}$ ). The major chemical species, that is, OM,  $\text{NO}_3^-$ ,  $\text{NH}_4^+$ , EC, and fine soil were lower by 43.1, 20.7, 20.6, 25.0, and 40.8% during the NCCPC-control period, respectively compared with samples taken after the controls were removed. Comparisons for only those days with stable meteorological conditions showed that the control versus non-control differences in  $\text{PM}_{2.5}$  (43.4%),  $\text{NO}_3^-$  (25.9%), OM (68.1%), EC (40.0%), and fine soil (58.7%) were larger compared with those for all days. Overall, these results indicate that control measures were effective in reducing fine particle pollution. Results of a PMF receptor model showed that biomass burning (27.3%) was the largest contributor to  $\text{PM}_{2.5}$  mass during the non-control period, followed by secondary source (19.5%), industrial processes (17.2%), traffic-related emissions (15.4%), mineral dust (12.3%), and coal burning (8.3%). In contrast, secondary source (37.3%) was the largest contributor to  $\text{PM}_{2.5}$  mass during the NCCPC-control period, followed by biomass burning (21.6%), traffic-related emissions (14.8%), coal burning (14.1%), mineral dust (6.3%), and industrial processes (6.0%). The mass concentrations of  $\text{PM}_{2.5}$  contributed by traffic-related emissions, biomass burning, industrial processes, and mineral dust all were lower during the NCCPC-control period compared with the non-control period. However, there was no significant difference in  $\text{PM}_{2.5}$  mass from coal burning between these two periods, and a larger  $\text{PM}_{2.5}$  mass concentration of secondary source was found for the NCCPC-control period.

There were two pollution episodes (PE1: 25–27 October and PE2: 31 October–1 November) that occurred after the NCCPC, and the average  $\text{PM}_{2.5}$  mass concentrations during those events ( $117.5 \mu\text{g m}^{-3}$  for PE1 and  $124.5 \mu\text{g m}^{-3}$  for PE2) were more than double those when the controls were in place. For PE1, secondary source was the most important source for fine particles, accounting for 54.6% of  $\text{PM}_{2.5}$  mass.

删除的内容: particle formation

删除的内容: processes

删除的内容: were

删除的内容: industry

删除的内容: particles

删除的内容: particle formation

586 Aerosol  $\text{NO}_3^-$  showed the largest contribution to  $\text{PM}_{2.5}$  mass (26.8%), and the high RH during PE1 likely  
587 promoted aqueous reactions involving nitrate. In contrast, OM (31.8%) was the most abundant species in  
588  $\text{PM}_{2.5}$  during the PE2, and the PMF indicated that biomass burning was the largest source, accounting for  
589 36.0% of the  $\text{PM}_{2.5}$  mass. The WRF-Chem simulation showed that the BTH region contributed 73.6%  
590 and 46.9% of  $\text{PM}_{2.5}$  mass during the PE1 and PE2, respectively.

591 Calculations based on methods developed for the IMPROVE program indicated that OM was the largest  
592 contributor (43.5%) to the chemical  $b_{\text{ext}}$  during the non-control period, followed by  $\text{NH}_4\text{NO}_3$  (32.4%), EC  
593 (14.3%),  $(\text{NH}_4)_2\text{SO}_4$  (7.6%), and fine soil (2.2%). During the NCCPC-control period,  $\text{NH}_4\text{NO}_3$  accounted  
594 for 36.7% of  $b_{\text{ext}}$ , and that was followed by OM (33.3%), EC (16.2%),  $(\text{NH}_4)_2\text{SO}_4$  (11.9%), and fine soil  
595 (1.9%). The TUV model showed that the estimated average DRF ( $-14.0 \pm 3.0 \text{ W m}^{-2}$ ) at the surface during  
596 the NCCPC-control period ~~was 27.5% less negative than in the non-control period ( $-19.3 \pm 8.6 \text{ W m}^{-2}$ )~~,  
597 and this is consistent with the lower  $\text{PM}_{2.5}$  loadings during the NCCPC-control period. Furthermore, EC  
598 had the largest (most negative) influence on DRF at the surface during the non-control period; the EC  
599 DRF value of  $-13.4 \text{ W m}^{-2}$  was followed by OM ( $-3.0 \text{ W m}^{-2}$ ),  $\text{NH}_4\text{NO}_3$  ( $-2.2 \text{ W m}^{-2}$ ),  $(\text{NH}_4)_2\text{SO}_4$  ( $-0.5 \text{ W}$   
600  $\text{m}^{-2}$ ), and fine soil ( $-0.15 \text{ W m}^{-2}$ ). The DRF values caused by EC,  $\text{NH}_4\text{NO}_3$ , OM, and fine soil when the  
601 controls were in place were lower by -10.1, -1.7, -1.6, and  $-0.09 \text{ W m}^{-2}$ , respectively, compared with the  
602 non-control period, and the corresponding percent reductions were 24.6, 22.7, 46.7, and 40.0%. The  
603 results suggest that the short-term mitigation measures during the NCCPC-control period were effective  
604 in reducing fine particle pollution and those actions also had radiative effects sufficient to affect surface  
605 temperature.

删除的内容: is

#### 606 Author contribution

607 QW and JC designed the research. QW, SL, WD, YW, JT, YZ, and MW carried out the measurements.

608 QW and NL performed the analysis, and QW wrote the paper. All the authors commented on the paper.

#### 609 **Acknowledgments**

610 This work was supported by the National Research Program for Key Issues in Air Pollution Control  
611 (DQGG0105) and the National Natural Science Foundation of China (41503118 and 41661144020). The  
612 authors are grateful to the staff from Xianghe Atmospheric Observatory for their assistance with field  
613 sampling.

615 **References**

- 616 Amil, N., Latif, M. T., Khan, M. F., and Mohamad, M.: Seasonal variability of PM<sub>2.5</sub> composition and  
617 sources in the Klang Valley urban-industrial environment, *Atmos. Chem. Phys.*, 16, 5357–5381,  
618 <https://doi.org/10.5194/acp-16-5357-2016>, 2016.
- 619 Bei, N., Li, G., and Molina, L. T.: Uncertainties in SOA simulations due to meteorological uncertainties  
620 in Mexico City during MILAGRO-2006 field campaign, *Atmos. Chem. Phys.*, 12, 11295–11308,  
621 <https://doi.org/10.5194/acp-16-5357-2016>, 2012.
- 622 Bei, N., Wu, J., Elser, M., Feng, T., Cao, J., El-Haddad, I., Li, X., Huang, R., Li, Z., Long, X., Xing, L.,  
623 Zhao, S., Tie, X., Prévôt, A. S. H., and Li, G.: Impacts of meteorological uncertainties on the haze  
624 formation in Beijing–Tianjin–Hebei (BTH) during wintertime: a case study, *Atmos. Chem. Phys.*,  
625 17, 14579–14591, <https://doi.org/10.5194/acp-17-14579-2017>, 2017.
- 626 Bukowiecki, N., Hill, M., Gehrig, R., Zwicky, C. N., Lienemann, P., Hegedüs, F., Falkenberg, G.,  
627 Weingartner, E., and Baltensperger, U.: Trace metals in ambient air: hourly size-segregated mass  
628 concentrations determined by synchrotron-XRF, *Environ. Sci. Technol.*, 39, 5754–5762,  
629 doi:10.1021/es048089m, 2005.
- 630 Canonaco, F., Slowik, J. G., Baltensperger, U., and Prévôt, A. S. H.: Seasonal differences in oxygenated  
631 organic aerosol composition: implications for emissions sources and factor analysis, *Atmos. Chem.*  
632 *Phys.*, 15, 6993–7002, <https://doi.org/10.5194/acp-15-6993-2015>, 2015.
- 633 Cao, J. J., Wang, Q. Y., Chow, J. C., Watson, J. G., Tie, X. X., Shen, Z. X., Wang, P., and An, Z. S.:  
634 Impacts of aerosol compositions on visibility impairment in Xi'an, China, *Atmos. Environ.*, 59, 559–  
635 566, <https://doi.org/10.1016/j.atmosenv.2012.05.036>, 2012.
- 636 Cao, J. J., Lee, S. C., Ho, K. F., Zhang, X. Y., Zou, S. C., Fung, K., Chow, J. C., and Watson, J. G.:  
637 Characteristics of carbonaceous aerosol in Pearl River Delta Region, China during 2001 winter  
638 period, *Atmos. Environ.*, 37, 1451–1460, [https://doi.org/10.1016/S1352-2310\(02\)01002-6](https://doi.org/10.1016/S1352-2310(02)01002-6), 2003.
- 639 Cao, J. J., Wu, F., Chow, J. C., Lee, S. C., Li, Y., Chen, S. W., An, Z. S., Fung, K. K., Watson, J. G., Zhu,  
640 C. S., and Liu, S. X.: Characterization and source apportionment of atmospheric organic and  
641 elemental carbon during fall and winter of 2003 in Xi'an, China, *Atmos. Chem. Phys.*, 5, 3127–3137,  
642 <https://doi.org/10.5194/acp-5-3127-2005>, 2005.
- 643 Chalbot, M. C., McElroy, B., and Kavouras, I. G.: Sources, trends and regional impacts of fine particulate  
644 matter in southern Mississippi valley: significance of emissions from sources in the Gulf of Mexico  
645 coast, *Atmos. Chem. Phys.*, 13, 3721–3732, <https://doi.org/10.5194/acp-13-3721-2013>, 2013.
- 646 Chen, J., Li, C., Ristovski, Z., Milic, A., Gu, Y., Islam, M. S., Wang, S., Hao, J., Zhang, H., He, C., Guo,  
647 H., Fu, H., Miljevic, B., Morawska, L., Thai, P., Lam, Y. F., Pereira, G., Ding, A., Huang, X., and  
648 Dumka, U. C.: A review of biomass burning: Emissions and impacts on air quality, health and  
649 climate in China, *Sci. Total Environ.*, 579, 1000–1034,  
650 <https://doi.org/10.1016/j.scitotenv.2016.11.025>, 2017.
- 651 Chen, Y., Xie, S. D., Luo, B., and Zhai, C. Z.: Particulate pollution in urban Chongqing of southwest  
652 China: Historical trends of variation, chemical characteristics and source apportionment, *Sci. Total*  
653 *Environ.*, 584–585, 523–534, <https://doi.org/10.1016/j.scitotenv.2017.01.060>, 2017.
- 654 Cheung, K., Daher, N., Shafer, M. M., Ning, Z., Schauer, J. J., and Sioutas, C.: Diurnal trends in coarse  
655 particulate matter composition in the Los Angeles Basin, *J. Environ. Monit.*, 13, 3277–3287, doi:  
656 10.1039/c1em10296f, 2011.
- 657 Chow, J. C., Watson, J. G., Chen, L. W. A., Chang, M. C. O., Robinson, N. F., Trimble, D., and Kohl, S.:  
658 The IMPROVE\_A Temperature Protocol for Thermal/Optical Carbon Analysis: Maintaining  
659 Consistency with a Long-Term Database, *J. Air Waste Manage. Assoc.*, 57, 1014–1023,  
660 <https://doi.org/10.3155/1047-3289.57.9.1014>, 2007.

661 Draxler, R. R. and Rolph, G. D.: HYSPLIT (HYbrid Single-Particle Lagrangian Integrated Trajectory),  
662 Silver Spring, MD, Model access via NOAA ARL READY Website:  
663 <http://www.arl.noaa.gov/ready/hysplit4.html>NOAA Air Resources Laboratory (last access: February  
664 2018), 2003

665 Du, H., Kong, L., Cheng, T., Chen, J., Du, J., Li, L., Xia, X., Leng, C., and Huang, G.: Insights into  
666 summertime haze pollution events over Shanghai based on online water-soluble ionic composition  
667 of aerosols, *Atmos. Environ.*, 45, 5131–5137, <https://doi.org/10.1016/j.atmosenv.2011.06.027>, 2011.

668 Duan, J., and Tan, J.: Atmospheric heavy metals and Arsenic in China: Situation, sources and control  
669 policies, *Atmos. Environ.*, 74, 93–101, <https://doi.org/10.1016/j.atmosenv.2013.03.031>, 2013.

670 Elser, M., Huang, R. J., Wolf, R., Slowik, J. G., Wang, Q. Y., Canonaco, F., Li, G., Bozzetti, C.,  
671 Daellenbach, K. R., Huang, Y., Zhang, R., Li, Z., Cao, J., Baltensperger, U., El-Haddad, I., and  
672 Prévôt, A. S. H.: New insights into PM<sub>2.5</sub> chemical composition and sources in two major cities in  
673 China during extreme haze events using aerosol mass spectrometry, *Atmos. Chem. Phys.*, 16, 3207–  
674 3225, <https://doi.org/10.5194/acp-16-3207-2016>, 2016.

675 Emmons, L. K., Walters, S., Hess, P. G., Lamarque, J. F., Pfister, G. G., Fillmore, D., Granier, C.,  
676 Guenther, A., Kinnison, D., Laepple, T., Orlando, J., Tie, X., Tyndall, G., Wiedinmyer, C.,  
677 Baughcum, S. L., and Kloster, S.: Description and evaluation of the Model for Ozone and Related  
678 chemical Tracers, version 4 (MOZART-4), *Geosci. Model Dev.*, 3, 43–67,  
679 <https://doi.org/10.5194/gmd-3-43-2010>, 2010.

680 Feng, S. L., Gao, D., Liao, F., Zhou, F. R., and Wang, X. M.: The health effects of ambient PM<sub>2.5</sub> and  
681 potential mechanisms, *Ecotox. Environ. Safe.*, 128, 67–74,  
682 <https://doi.org/10.1016/j.ecoenv.2016.01.030>, 2016.

683 Gao, Y., Liu, X., Zhao, C., and Zhang, M.: Emission controls versus meteorological conditions in  
684 determining aerosol concentrations in Beijing during the 2008 Olympic Games, *Atmos. Chem. Phys.*,  
685 11, 12437–12451, <https://doi.org/10.5194/acp-11-12437-2011>, 2011.

686 Guo, S., Hu, M., Guo, Q., Zhang, X., Schauer, J. J., and Zhang, R.: Quantitative evaluation of emission  
687 controls on primary and secondary organic aerosol sources during Beijing 2008 Olympics, *Atmos.*  
688 *Chem. Phys.*, 13, 8303–8314, <https://doi.org/10.5194/acp-13-8303-2013>, 2013.

689 Hallquist, M., Wenger, J. C., Baltensperger, U., Rudich, Y., Simpson, D., Claeys, M., Dommen, J.,  
690 Donahue, N. M., George, C., Goldstein, A. H., Hamilton, J. F., Herrmann, H., Hoffmann, T., Iinuma,  
691 Y., Jang, M., Jenkin, M. E., Jimenez, J. L., Kiendler-Scharr, A., Maenhaut, W., McFiggans, G.,  
692 Mentel, T. F., Monod, A., Prévôt, A. S. H., Seinfeld, J. H., Surratt, J. D., Szmigielski, R., and Wildt,  
693 J.: The formation, properties and impact of secondary organic aerosol: current and emerging issues,  
694 *Atmos. Chem. Phys.*, 9, 5155–5236, <https://doi.org/10.5194/acp-9-5155-2009>, 2009.

695 Han, X., Guo, Q., Liu, C., Strauss, H., Yang, J., Hu, J., Wei, R., Tian, L., Kong, J., and Peters, M.: Effect  
696 of the pollution control measures on PM<sub>2.5</sub> during the 2015 China Victory Day Parade: Implication  
697 from water-soluble ions and sulfur isotope, *Environ. Pollut.*, 218, 230–241,  
698 <https://doi.org/10.1016/j.envpol.2016.06.038>, 2016.

699 Hsu, S.-C., Liu, S. C., Huang, Y.-T., Chou, C. C. K., Lung, S. C. C., Liu, T.-H., Tu, J.-Y., and Tsai, F.:  
700 Long-range southeastward transport of Asian biosmoke pollution: Signature detected by aerosol  
701 potassium in Northern Taiwan, *J. Geophys. Res.-Atmos.*, 114, D14301, doi:10.1029/2009JD011725,  
702 2009.

703 Huang, X., Liu, Z., Liu, J., Hu, B., Wen, T., Tang, G., Zhang, J., Wu, F., Ji, D., Wang, L., and Wang, Y.:  
704 Chemical characterization and source identification of PM<sub>2.5</sub> at multiple sites in the Beijing-Tianjin-  
705 Hebei region, China, *Atmos. Chem. Phys.*, 17, 12941–12962, [https://doi.org/10.5194/acp-17-12941-](https://doi.org/10.5194/acp-17-12941-2017)  
706 2017, 2017.

707 Khan, M. F., Sulong, N. A., Latif, M. T., Nadzir, M. S. M., Amil, N., Hussain, D. F. M., Lee, V., Hosaini,  
708 P. N., Shaharom, S., Yusoff, N. A. Y. M., Hoque, H. M. S., Chung, J. X., Sahani, M., Mohd Tahir,  
709 N., Juneng, L., Maulud, K. N. A., Abdullah, S. M. S., Fujii, Y., Tohno, S., and Mizohata, A.:  
710 Comprehensive assessment of PM<sub>2.5</sub> physicochemical properties during the Southeast Asia dry  
711 season (southwest monsoon), *J. Geophys. Res.-Atmos.*, 121, 14589–14611,  
712 doi:10.1002/2016JD025894, 2016a.

713 Khan, M. F., Latif, M. T., Saw, W. H., Amil, N., Nadzir, M. S. M., Sahani, M., Tahir, N. M., and Chung,  
714 J. X.: Fine particulate matter in the tropical environment: monsoonal effects, source apportionment,  
715 and health risk assessment, *Atmos. Chem. Phys.*, 16, 597–617, [https://doi.org/10.5194/acp-16-597-](https://doi.org/10.5194/acp-16-597-2016)  
716 2016, 2016b.

717 Kuang, B. Y., Lin, P., Huang, X. H. H., and Yu, J. Z.: Sources of humic-like substances in the Pearl River  
718 Delta, China: positive matrix factorization analysis of PM<sub>2.5</sub> major components and source markers,  
719 *Atmos. Chem. Phys.*, 15, 1995–2008, <https://doi.org/10.5194/acp-15-1995-2015>, 2015.

720 Lecoeur, E., Seigneur, C., Page, C., and Terray, L.: A statistical method to estimate PM<sub>2.5</sub> concentrations  
721 from meteorology and its application to the effect of climate change, *J. Geophys. Res.-Atmos.*, 119,  
722 3537–3585, doi:10.1002/2013JD021172, 2014.

723 Li, G., Bei, N., Tie, X., and Molina, L. T.: Aerosol effects on the photochemistry in Mexico City during  
724 MCMA-2006/MILAGRO campaign, *Atmos. Chem. Phys.*, 11, 5169–5182,  
725 <https://doi.org/10.5194/acp-11-5169-2011>, 2011a.

726 Li, G., Zavala, M., Lei, W., Tsimpidi, A. P., Karydis, V. A., Pandis, S. N., Canagaratna, M. R., and Molina,  
727 L. T.: Simulations of organic aerosol concentrations in Mexico City using the WRF-CHEM model  
728 during the MCMA-2006/MILAGRO campaign, *Atmos. Chem. Phys.*, 11, 3789–3809,  
729 <https://doi.org/10.5194/acp-11-3789-2011>, 2011b.

730 Li, G., Lei, W., Bei, N., and Molina, L. T.: Contribution of garbage burning to chloride and PM<sub>2.5</sub> in  
731 Mexico City, *Atmos. Chem. Phys.*, 12, 8751–8761, <https://doi.org/10.5194/acp-12-8751-2012>, 2012.

732 Li, J., Xie, S. D., Zeng, L. M., Li, L. Y., Li, Y. Q., and Wu, R. R.: Characterization of ambient volatile  
733 organic compounds and their sources in Beijing, before, during, and after Asia-Pacific Economic  
734 Cooperation China 2014, *Atmos. Chem. Phys.*, 15, 7945–7959, [https://doi.org/10.5194/acp-15-](https://doi.org/10.5194/acp-15-7945-2015)  
735 7945-2015, 2015.

736 Li, J., and Han, Z.: A modeling study of severe winter haze events in Beijing and its neighboring regions,  
737 *Atmos. Res.*, 170, 87–97, <https://doi.org/10.1016/j.atmosres.2015.11.009>, 2016.

738 Li, X., He, K., Li, C., Yang, F., Zhao, Q., Ma, Y., Cheng, Y., Ouyang, W., and Chen, G.: PM<sub>2.5</sub> mass,  
739 chemical composition, and light extinction before and during the 2008 Beijing Olympics, *J. Geophys.*  
740 *Res.-Atmos.*, 118, 12158–12167, doi:10.1002/2013JD020106, 2013.

741 Liang, P., Zhu, T., Fang, Y., Li, Y., Han, Y., Wu, Y., Hu, M., and Wang, J.: The role of meteorological  
742 conditions and pollution control strategies in reducing air pollution in Beijing during APEC 2014  
743 and Victory Parade 2015, *Atmos. Chem. Phys.*, 17, 13921–13940, [https://doi.org/10.5194/acp-17-](https://doi.org/10.5194/acp-17-13921-2017)  
744 13921-2017, 2017.

745 Lim, H.-J., and Turpin, B. J.: Origins of primary and secondary organic aerosol in Atlanta: Results of  
746 time-resolved measurements during the Atlanta Supersite Experiment, *Environ. Sci. Technol.*, 36,  
747 4489–4496, doi:10.1021/es0206487, 2002.

748 Lin, H., Liu, T., Fang, F., Xiao, J., Zeng, W., Li, X., Guo, L., Tian, L., Schoutman, M., Stamatakis, K. A.,  
749 Qian, Z., and Ma, W.: Mortality benefits of vigorous air quality improvement interventions during  
750 the periods of APEC Blue and Parade Blue in Beijing, China, *Environ. Pollut.*, 220, 222–227,  
751 <https://doi.org/10.1016/j.envpol.2016.09.041>, 2017.

752 Lin, Y. C., Tsai, C. J., Wu, Y. C., Zhang, R., Chi, K. H., Huang, Y. T., Lin, S. H., and Hsu, S. C.:  
753 Characteristics of trace metals in traffic-derived particles in Hsuehshan Tunnel, Taiwan: size

distribution, potential source, and fingerprinting metal ratio, *Atmos. Chem. Phys.*, 15, 4117–4130, <https://doi.org/10.5194/acp-15-4117-2015>, 2015.

Liu, B., Wu, J., Zhang, J., Wang, L., Yang, J., Liang, D., Dai, Q., Bi, X., Feng, Y., Zhang, Y., and Zhang, Q.: Characterization and source apportionment of PM<sub>2.5</sub> based on error estimation from EPA PMF 5.0 model at a medium city in China, *Environ. Pollut.*, 222, 10–22, <https://doi.org/10.1016/j.envpol.2017.01.005>, 2017.

Madronich, S.: UV radiation in the natural and perturbed atmosphere, In: M. Tevini, Ed., *UV-B Radiation and Ozone Depletion*, Lewis Publishers, London, pp. 17–69, 1993.

Malm William, C., Day Derek, E., Kreidenweis Sonia, M., Collett Jeffrey, L., and Lee, T.: Humidity-dependent optical properties of fine particles during the Big Bend Regional Aerosol and Visibility Observational Study, *J. Geophys. Res.-Atmos.*, 108(D9), 4279, doi:10.1029/2002JD002998, 2003.

Men, C., Liu, R., Xu, F., Wang, Q., Guo, L., and Shen, Z.: Pollution characteristics, risk assessment, and source apportionment of heavy metals in road dust in Beijing, China, *Sci. Total Environ.*, 612, 138–147, <https://doi.org/10.1016/j.scitotenv.2017.08.123>, 2018.

Milando, C., Huang, L., and Batterman, S.: Trends in PM<sub>2.5</sub> emissions, concentrations and apportionments in Detroit and Chicago, *Atmos. Environ.*, 129, 197–209, <https://doi.org/10.1016/j.atmosenv.2016.01.012>, 2016.

National Bureau of Statistics (NBS): China Statistical Yearbook 2013, China Statistics Press, Beijing, 2013a (in Chinese).

Norris, G., Duvall, R., Brown, S., and Bai, S.: EPA Positive Matrix Factorization (PMF) 5.0 fundamentals and User Guide Prepared for the US Environmental Protection Agency Office of Research and Development, Washington, DC, Inc., Petaluma, 2014.

Paatero, P., and Tapper, U.: Positive matrix factorization: A non-negative factor model with optimal utilization of error estimates of data values, *Environmetrics*, 5, 111–126, <https://doi.org/10.1002/env.3170050203>, 2006.

Palancar, G. G., and Toselli, B. M.: Effects of meteorology and tropospheric aerosols on UV-B radiation: a 4-year study, *Atmos. Environ.*, 38, 2749–2757, <https://doi.org/10.1016/j.atmosenv.2004.01.036>, 2004.

Pipal, A. S., Kulshrestha, A., and Taneja, A.: Characterization and morphological analysis of airborne PM<sub>2.5</sub> and PM<sub>10</sub> in Agra located in north central India, *Atmos. Environ.*, 45, 3621–3630, <https://doi.org/10.1016/j.atmosenv.2011.03.062>, 2011.

Pitchford, M., Malm, W., Schichtel, B., Kumar, N., Lowenthal, D., and Hand, J.: Revised algorithm for estimating light extinction from IMPROVE particle speciation data, *J. Air Waste Manage. Assoc.*, 57, 1326–1336, doi:10.3155/1047-3289.57.11.1326, 2007.

Pui, D. Y. H., Chen, S. C., and Zuo, Z. L.: PM<sub>2.5</sub> in China: Measurements, sources, visibility and health effects, and mitigation, *Particuology*, 13, 1–26, <https://doi.org/10.1016/j.partic.2013.11.001>, 2014.

Ran, L., Deng, Z. Z., Wang, P. C., and Xia, X. A.: Black carbon and wavelength-dependent aerosol absorption in the North China Plain based on two-year aethalometer measurements, *Atmos. Environ.*, 142, 132–144, <https://doi.org/10.1016/j.atmosenv.2016.07.014>, 2016.

Sammaritano, M. A., Bustos, D. G., Poblete, A. G., and Wannaz, E. D.: Elemental composition of PM<sub>2.5</sub> in the urban environment of San Juan, Argentina, *Environ. Sci. Pollut. Res.*, 25, 4197–4203, <https://doi.org/10.1007/s11356-017-0793-5>, 2018.

Sun, Y., Jiang, Q., Wang, Z., Fu, P., Li, J., Yang, T., and Yin, Y.: Investigation of the sources and evolution processes of severe haze pollution in Beijing in January 2013, *J. Geophys. Res.-Atmos.*, 119, 4380–4398, doi:10.1002/2014JD021641, 2014.

799 Tang, G., Zhu, X., Hu, B., Xin, J., Wang, L., Münkel, C., Mao, G., and Wang, Y.: Impact of emission  
800 controls on air quality in Beijing during APEC 2014: lidar ceilometer observations, *Atmos. Chem.*  
801 *Phys.*, 15, 12667–12680, <https://doi.org/10.5194/acp-15-12667-2015>, 2015.

802 Tao, J., Gao, J., Zhang, L., Zhang, R., Che, H., Zhang, Z., Lin, Z., Jing, J., Cao, J., and Hsu, S. C.: PM<sub>2.5</sub>  
803 pollution in a megacity of southwest China: source apportionment and implication, *Atmos. Chem.*  
804 *Phys.*, 14, 8679–8699, <https://doi.org/10.5194/acp-14-8679-2014>, 2014.

805 Tao, J., Gao, J., Zhang, L., Wang, H., Qiu, X., Zhang, Z., Wu, Y., Chai, F., and Wang, S.: Chemical and  
806 optical characteristics of atmospheric aerosols in Beijing during the Asia-Pacific Economic  
807 Cooperation China 2014, *Atmos. Environ.*, 144, 8–16,  
808 <https://doi.org/10.1016/j.atmosenv.2016.08.067>, 2016.

809 Tao, J., Zhang, L. M., Cao, J. J., and Zhang, R. J.: A review of current knowledge concerning PM<sub>2.5</sub>  
810 chemical composition, aerosol optical properties and their relationships across China, *Atmos. Chem.*  
811 *Phys.*, 17, 9485–9518, <https://doi.org/10.5194/acp-17-9485-2017>, 2017.

812 Tie, X., Huang, R.-J., Dai, W., Cao, J., Long, X., Su, X., Zhao, S., Wang, Q., and Li, G.: Effect of heavy  
813 haze and aerosol pollution on rice and wheat productions in China, *Sci. Rep.*, 6, 29612,  
814 doi:10.1038/srep29612, 2016.

815 Wang, J., Wang, G., Gao, J., Wang, H., Ren, Y., Li, J., Zhou, B., Wu, C., Zhang, L., Wang, S., and Chai,  
816 F.: Concentrations and stable carbon isotope compositions of oxalic acid and related SOA in Beijing  
817 before, during, and after the 2014 APEC, *Atmos. Chem. Phys.*, 17, 981–992,  
818 <https://doi.org/10.5194/acp-17-981-2017>, 2017.

819 Wang, Q. Q., He, X., Huang, X. H. H., Griffith, S. M., Feng, Y., Zhang, T., Zhang, Q., Wu, D., and Yu,  
820 J. Z.: Impact of secondary organic aerosol tracers on tracer-based source apportionment of organic  
821 carbon and PM<sub>2.5</sub>: A case study in the Pearl River Delta, China, *Earth and Space Chemistry*, 1, 562–  
822 571, doi:10.1021/acsearthspacechem.7b00088, 2017.

823 Wang, Q. Y., Huang, R.-J., Cao, J., Tie, X., Shen, Z., Zhao, S., Han, Y., Li, G., Li, Z., Ni, H., Zhou, Y.,  
824 Wang, M., Chen, Y., and Su, X.: Contribution of regional transport to the black carbon aerosol during  
825 winter haze period in Beijing, *Atmos. Environ.*, 132, 11–18,  
826 <http://dx.doi.org/10.1016/j.atmosenv.2016.02.031>, 2016a.

827 Wang, Q. Y., Huang, R.-J., Zhao, Z., Cao, J., Ni, H., Tie, X., Zhao, S., Su, X., Han, Y., Shen, Z., Wang,  
828 Y., Zhang, N., Zhou, Y., and Corbin, J. C.: Physicochemical characteristics of black carbon aerosol  
829 and its radiative impact in a polluted urban area of China, *J. Geophys. Res.-Atmos.*, 121, 12505–  
830 12519, doi:10.1002/2016JD024748, 2016b.

831 Wang, Q. Y., Cao, J., Han, Y., Tian, J., Zhang, Y., Pongpiachan, S., Zhang, Y., Li, L., Niu, X., Shen, Z.,  
832 Zhao, Z., Tipmanee, D., Bunsomboonsakul, S., Chen, Y., and Sun, J.: Enhanced light absorption due  
833 to the mixing state of black carbon in fresh biomass burning emissions, *Atmos. Environ.*, 180, 184–  
834 191, <https://doi.org/10.1016/j.atmosenv.2018.02.049>, 2018a.

835 Wang, Q. Y., Cao, J., Han, Y., Tian, J., Zhu, C., Zhang, Y., Zhang, N., Shen, Z., Ni, H., Zhao, S., and  
836 Wu, J.: Sources and physicochemical characteristics of black carbon aerosol from the southeastern  
837 Tibetan Plateau: internal mixing enhances light absorption, *Atmos. Chem. Phys.*, 18, 4639–4656,  
838 <https://doi.org/10.5194/acp-18-4639-2018>, 2018b.

839 Wang, S., Zhao, M., Xing, J., Wu, Y., Zhou, Y., Lei, Y., He, K., Fu, L., and Hao, J.: Quantifying the air  
840 pollutants emission reduction during the 2008 Olympic Games in Beijing, *Environ. Sci. Technol.*,  
841 44, 2490–2496, doi:10.1021/es9028167, 2010.

842 Wang, W., Primbs, T., Tao, S., and Simonich, S. L. M.: Atmospheric particulate matter pollution during  
843 the 2008 Beijing Olympics, *Environ. Sci. Technol.*, 43, 5314–5320, doi:10.1021/es9007504, 2009.

844 Wang, Z., Li, Y., Chen, T., Li, L., Liu, B., Zhang, D., Sun, F., Wei, Q., Jiang, L., and Pan, L.: Changes  
845 in atmospheric composition during the 2014 APEC conference in Beijing, *J. Geophys. Res.-Atmos.*,  
846 120, 12695–12707, doi:10.1002/2015JD023652, 2015.

847 Watson, J. G.: Visibility: Science and regulation, *J. Air Waste Manage. Assoc.*, 52, 628–713,  
848 <https://doi.org/10.1080/10473289.2002.10470813>, 2002.

849 Xia, X., Li, Z., Wang, P., Chen, H., and Cribb, M.: Estimation of aerosol effects on surface irradiance  
850 based on measurements and radiative transfer model simulations in northern China, *J. Geophys.*  
851 *Res.- Atmos.*, 112, D22S10, doi:10.1029/2006JD008337, 2007a.

852 Xia, X., Li, Z., Holben, B., Wang, P., Eck, T., Chen, H., Cribb, M., and Zhao, Y.: Aerosol optical  
853 properties and radiative effects in the Yangtze Delta region of China, *J. Geophys. Res.- Atmos.*, 112,  
854 D22S12, doi:10.1029/2007JD008859, 2007b.

855 Xiao, S., Wang, Q., Cao, J., Huang, R.-J., Chen, W., Han, Y., Xu, H., Liu, S., Zhou, Y., and Wang, P.:  
856 Long-term trends in visibility and impacts of aerosol composition on visibility impairment in Baoji,  
857 China, *Atmos. Res.*, 149, 88–95, <http://dx.doi.org/10.1016/j.atmosres.2014.06.006>, 2014.

858 Xie, R., Sabel, C. E., Lu, X., Zhu, W. M., Kan, H. D., Nielsen, C. P., and Wang, H. K.: Long-term trend  
859 and spatial pattern of PM<sub>2.5</sub> induced premature mortality in China, *Environ. Int.*, 97, 180–186,  
860 <https://doi.org/10.1016/j.envint.2016.09.003>, 2016.

861 Xu, H. M., Cao, J. J., Ho, K. F., Ding, H., Han, Y. M., Wang, G. H., Chow, J. C., Watson, J. G., Khol, S.  
862 D., Qiang, J., and Li, W. T.: Lead concentrations in fine particulate matter after the phasing out of  
863 leaded gasoline in Xi'an, China, *Atmos. Environ.*, 46, 217–224,  
864 <https://doi.org/10.1016/j.atmosenv.2011.09.078>, 2012.

865 Xu, J., Bergin, M. H., and Greenwald, R.: Direct aerosol radiative forcing in the Yangtze delta region of  
866 China: Observation and model estimation, *J. Geophys. Res.-Atmos.*, 108(D2), 4060,  
867 doi:10.1029/2002JD002550, 2003.

868 Xu, W., Song, W., Zhang, Y., Liu, X., Zhang, L., Zhao, Y., Liu, D., Tang, A., Yang, D., Wang, D., Wen,  
869 Z., Pan, Y., Fowler, D., Collett Jr, J. L., Erismann, J. W., Goulding, K., Li, Y., and Zhang, F.: Air  
870 quality improvement in a megacity: implications from 2015 Beijing Parade Blue pollution control  
871 actions, *Atmos. Chem. Phys.*, 17, 31–46, <https://doi.org/10.5194/acp-17-31-2017>, 2017.

872 Xu, W. Q., Sun, Y. L., Chen, C., Du, W., Han, T. T., Wang, Q. Q., Fu, P. Q., Wang, Z. F., Zhao, X. J.,  
873 Zhou, L. B., Ji, D. S., Wang, P. C., and Worsnop, D. R.: Aerosol composition, oxidation properties,  
874 and sources in Beijing: results from the 2014 Asia-Pacific Economic Cooperation summit study,  
875 *Atmos. Chem. Phys.*, 15, 13681–13698, <https://doi.org/10.5194/acp-15-13681-2015>, 2015.

876 Yang, M., Howell, S. G., Zhuang, J., and Huebert, B. J.: Attribution of aerosol light absorption to black  
877 carbon, brown carbon, and dust in China—interpretations of atmospheric measurements during EAST-  
878 AIRE, *Atmos. Chem. Phys.*, 9, 2035–2050, <https://doi.org/10.5194/acp-9-2035-2009>, 2009.

879 Zhang, R., Jing, J., Tao, J., Hsu, S. C., Wang, G., Cao, J., Lee, C. S. L., Zhu, L., Chen, Z., Zhao, Y., and  
880 Shen, Z.: Chemical characterization and source apportionment of PM<sub>2.5</sub> in Beijing: seasonal  
881 perspective, *Atmos. Chem. Phys.*, 13, 7053–7074, doi:10.5194/acp-13-7053-2013, 2013.

882 Zhang, T., Cao, J. J., Tie, X. X., Shen, Z. X., Liu, S. X., Ding, H., Han, Y. M., Wang, G. H., Ho, K. F.,  
883 Qiang, J., and Li, W. T.: Water-soluble ions in atmospheric aerosols measured in Xi'an, China:  
884 Seasonal variations and sources, *Atmos. Res.*, 102, 110–119,  
885 <https://doi.org/10.1016/j.atmosres.2011.06.014>, 2011.

886 Zhang, Y., Lang, J., Cheng, S., Li, S., Zhou, Y., Chen, D., Zhang, H., and Wang, H.: Chemical  
887 composition and sources of PM<sub>1</sub> and PM<sub>2.5</sub> in Beijing in autumn, *Sci. Total Environ.*, 630, 72–82,  
888 <https://doi.org/10.1016/j.scitotenv.2018.02.151>, 2018.

889 Zheng, G., Duan, F., Ma, Y., Zhang, Q., Huang, T., Kimoto, T., Cheng, Y., Su, H., and He, K.: Episode-  
890 based evolution pattern analysis of haze pollution: Method development and results from Beijing,  
891 China, *Environ. Sci. Technol.*, 50, 4632–4641, doi:10.1021/acs.est.5b05593, 2016.

892 Zheng, G. J., Duan, F. K., Su, H., Ma, Y. L., Cheng, Y., Zheng, B., Zhang, Q., Huang, T., Kimoto, T.,  
893 Chang, D., Pöschl, U., Cheng, Y. F., and He, K. B.: Exploring the severe winter haze in Beijing: the  
894 impact of synoptic weather, regional transport and heterogeneous reactions, *Atmos. Chem. Phys.*,  
895 15, 2969–2983, <https://doi.org/10.5194/acp-15-2969-2015>, 2015.

896 Zhong, J., Zhang, X., Dong, Y., Wang, Y., Liu, C., Wang, J., Zhang, Y., and Che, H.: Feedback effects  
897 of boundary-layer meteorological factors on cumulative explosive growth of PM<sub>2.5</sub> during winter  
898 heavy pollution episodes in Beijing from 2013 to 2016, *Atmos. Chem. Phys.*, 18, 247–258,  
899 <https://doi.org/10.5194/acp-18-247-2018>, 2018.

900 Zong, Z., Wang, X., Tian, C., Chen, Y., Qu, L., Ji, L., Zhi, G., Li, J., and Zhang, G.: Source apportionment  
901 of PM<sub>2.5</sub> at a regional background site in North China using PMF linked with radiocarbon analysis:  
902 insight into the contribution of biomass burning, *Atmos. Chem. Phys.*, 16, 11249–11265,  
903 <https://doi.org/10.5194/acp-16-11249-2016>, 2016.

904 Zhou, Y., Wang, Q., Huang, R., Liu, S., Tie, X., Su, X., Niu, X., Zhao, Z., Ni, H., Wang, M., Zhang, Y.,  
905 and Cao, J.: Optical properties of aerosols and implications for radiative effects in Beijing during the  
906 Asia-Pacific Economic Cooperation Summit 2014, *J. Geophys. Res.-Atmos.*, 122, 10119–10132,  
907 <https://doi.org/10.1002/2017JD026997>, 2017.

908 Zhuang, B. L., Wang, T. J., Liu, J., Li, S., Xie, M., Yang, X. Q., Fu, C. B., Sun, J. N., Yin, C. Q., Liao, J.  
909 B., Zhu, J. L., and Zhang, Y.: Continuous measurement of black carbon aerosol in urban Nanjing of  
910 Yangtze River Delta, China, *Atmos. Environ.*, 89, 415–424,  
911 <https://doi.org/10.1016/j.atmosenv.2014.02.052>, 2014.

912

913 **Table 1** Summary of PM<sub>2.5</sub> and its major chemical components at Xianghe during the 19th  
 914 National Congress of the Communist Party of China (NCCPC)-control and non-control periods.

Components	Grand average ( $\mu\text{g m}^{-3}$ )	Control period ( $\mu\text{g m}^{-3}$ )	Non-control period ( $\mu\text{g m}^{-3}$ )	Change ratio <sup>a</sup> (%)
PM <sub>2.5</sub>	70.0	57.9 (63.7) <sup>b</sup>	84.1 (112.6)	31.2 (43.4)
NO <sub>3</sub> <sup>-</sup>	15.0	13.4 (18.0)	16.9 (24.3)	20.7 (25.9)
SO <sub>4</sub> <sup>2-</sup>	5.6	5.8 (7.6)	5.3 (6.6)	-9.4 (-15.2)
NH <sub>4</sub> <sup>+</sup>	6.0	5.4 (8.6)	6.8 (9.7)	20.6 (11.3)
Cl <sup>-</sup>	2.2	1.6 (1.5)	2.9 (3.4)	44.8 (55.9)
Organic matter	18.9	14.0 (9.5)	24.6 (29.8)	43.1 (68.1)
Elemental carbon	5.2	4.5 (4.5)	6.0 (7.5)	25.0 (40.0)
Trace elements	1.8	1.4 (1.2)	2.3 (3.0)	39.1 (60.0)
Fine soil	5.5	4.2 (2.6)	7.1 (6.3)	40.8 (58.7)

915 <sup>a</sup>([Non-control period]-[NCCPC-control period])/[Non-control period].

916 <sup>b</sup>Values in parentheses show the results for days with stable meteorological conditions (wind  
 917 speed < 0.4 m s<sup>-1</sup> and mixed layer height < 274 m).

918

919

### Figure Captions

920 **Figure 1.** Location of the Xianghe sampling site. The map was drawn using the ArcGIS.

921 **Figure 2.** (left) Daily variations in the contributions of chemical species to PM<sub>2.5</sub> mass during the  
922 campaign and (right) average contributions of chemical species during the 19th National Congress  
923 of the Communist Party of China (NCCPC)-control and non-control periods. PE1 and PE2 represent  
924 two pollution episodes.

925 **Figure 3.** Scatter plots showing the relationships between PM<sub>2.5</sub> mass concentrations and (a) wind speed  
926 and (b) mixed layer height.

927 **Figure 4.** (a) Source profiles for the six sources identified using the positive matrix factorization model  
928 version 5.0, (b) the mass concentrations of PM<sub>2.5</sub> contributed by each source, and (c) the average  
929 source contribution of each source to the PM<sub>2.5</sub> mass.

930 **Figure 5.** Average source contributions of (a) each positive matrix factorization source factor and (b)  
931 chemical species to the PM<sub>2.5</sub> mass during two pollution episodes (PE1 and PE2).

932 **Figure 6.** Correlations for (a) PM<sub>2.5</sub> mass concentrations versus molar ratios of NO<sub>3</sub><sup>-</sup> and NO<sub>2</sub> (NOR), (b)  
933 NOR versus relative humidity (RH), (c) the ratio of secondary organic aerosol to elemental carbon  
934 (SOA/EC) ratios versus Ox (O<sub>3</sub> + NO<sub>2</sub>), and (d) SOA/EC versus RH for all samples from the  
935 campaign.

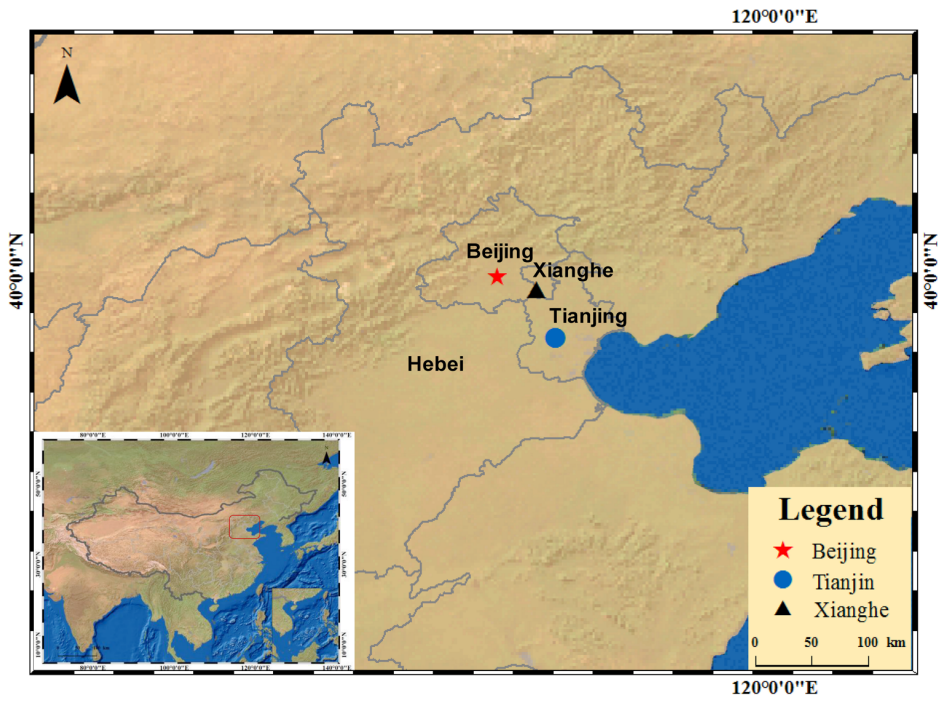
936 **Figure 7.** Three-day backward in time air mass trajectories (BT) arriving at 150 m above ground every  
937 hour from 31 October to 1 November 2017. The orange points represent fire counts that were derived  
938 from Moderate Resolution Imaging Spectroradiometer observations.

939 **Figure 8.** Surface weather charts for 08:00 (local time) over East Asia from 22 October to 2 November  
940 2017. The black triangles represent Xianghe.

941 **Figure 9.** Daily average PM<sub>2.5</sub> concentrations (μg m<sup>-3</sup>) simulated for the Beijing-Tianjin-Hebei region  
942 and surrounding areas from 25 October to 2 November 2017. The Weather Research and Forecasting  
943 model coupled to chemistry (WRF-Chem) model was used for the simulation.

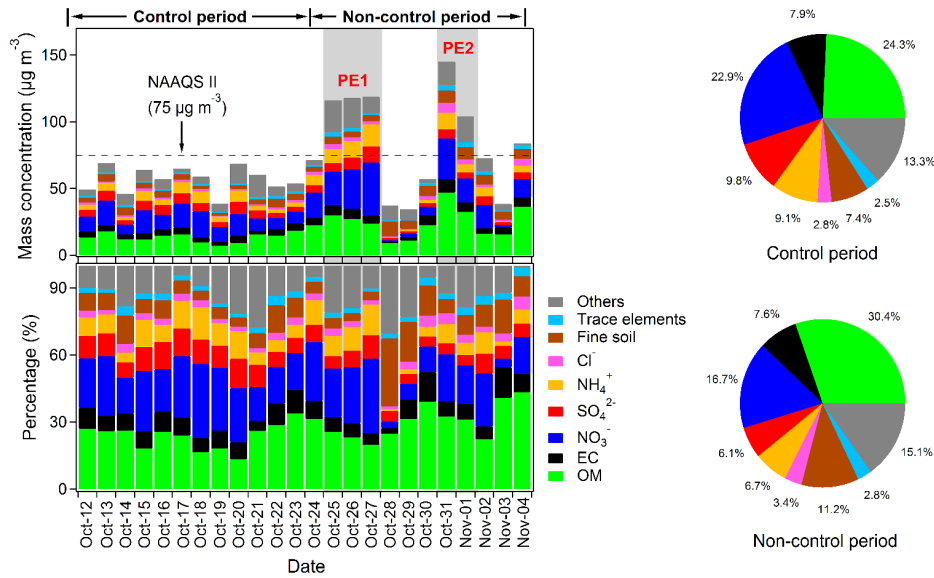
944 **Figure 10.** Average values of (a) light extinction coefficients (including light scattering and absorption)  
945 and (b) direct radiative forcing (DRF) at the surface contributed by each PM<sub>2.5</sub> chemical composition  
946 during the 19th National Congress of the Communist Party of China (NCCPC)-control and non-  
947 control periods.

948

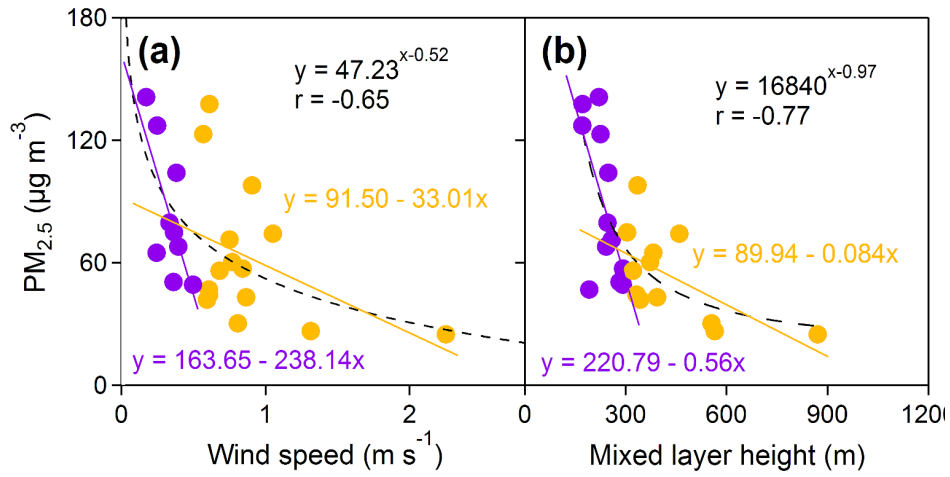


949  
950

951 **Figure 1.**

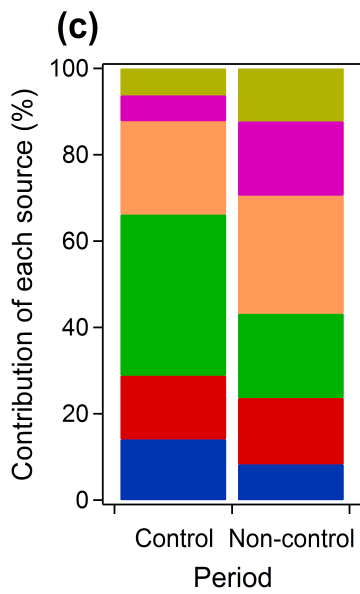
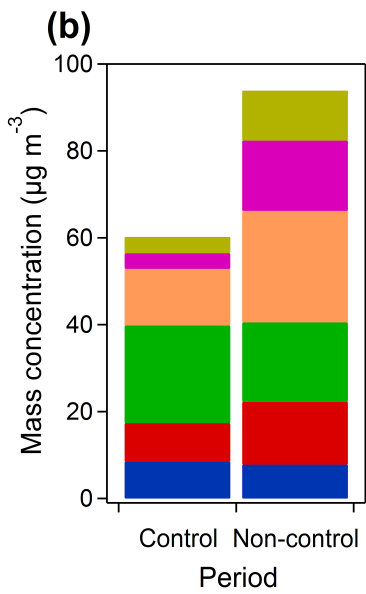
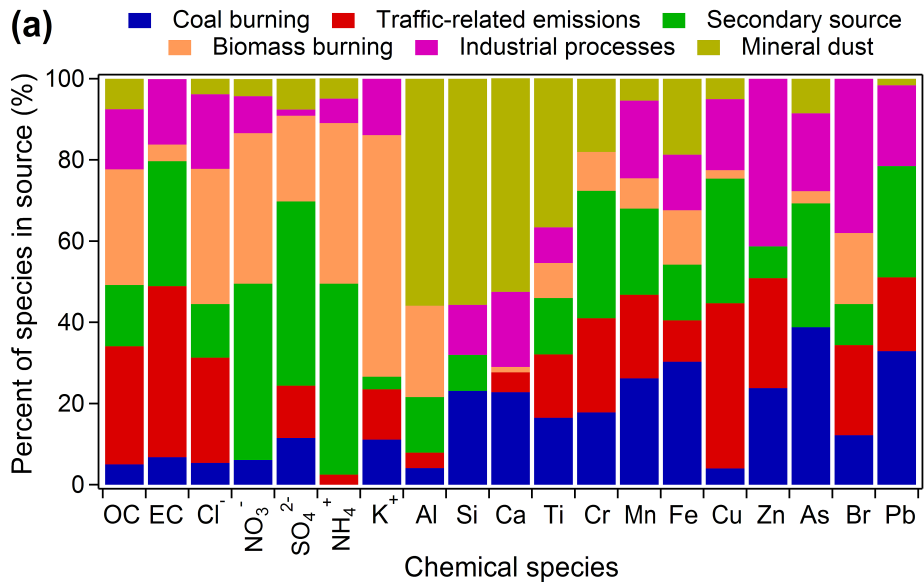


952  
953 **Figure 2.**  
954



955  
956  
957  
958

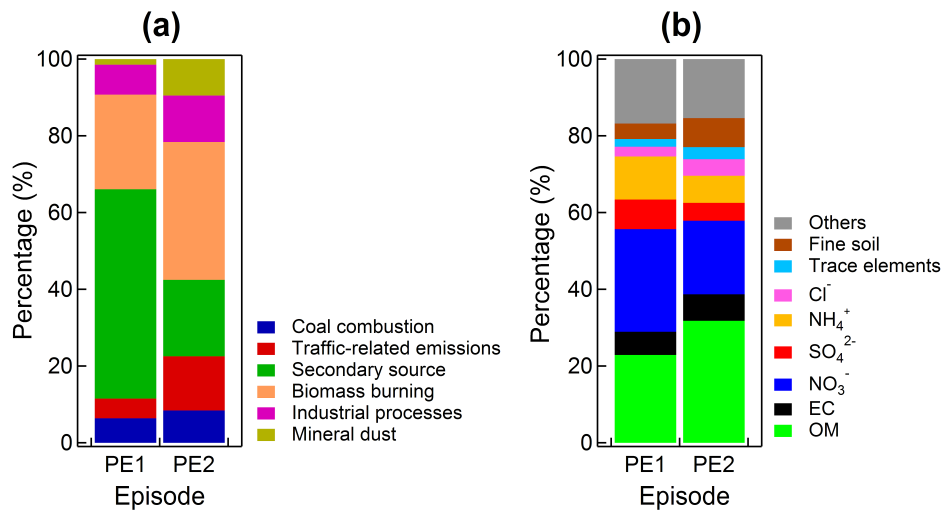
Figure 3.



959

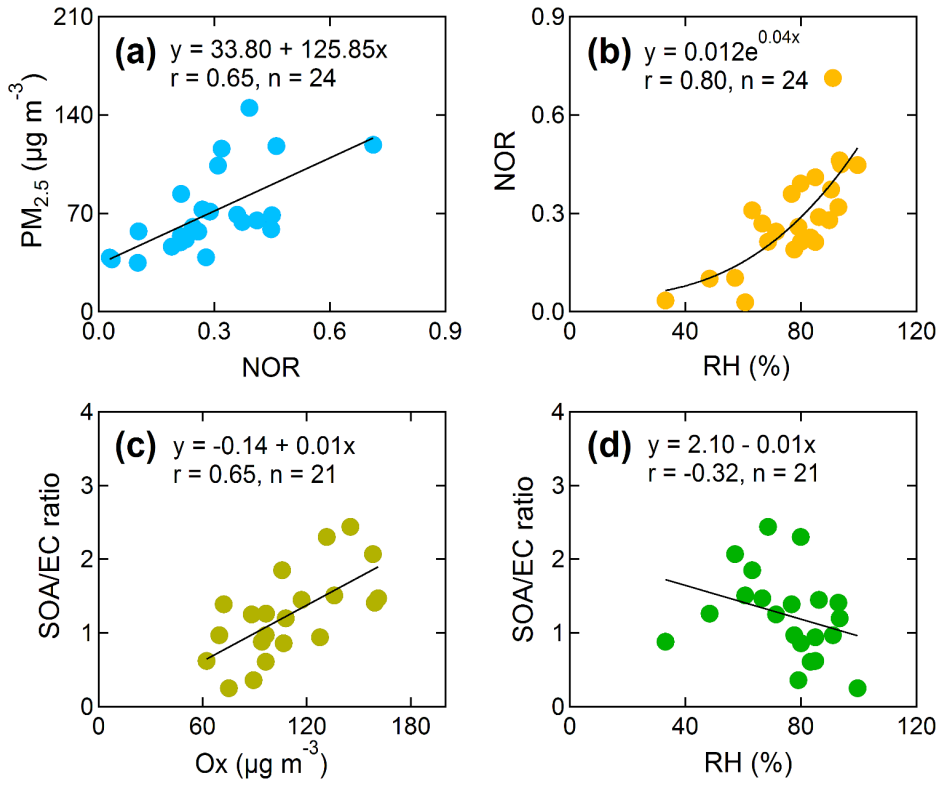
960

961 **Figure 4.**



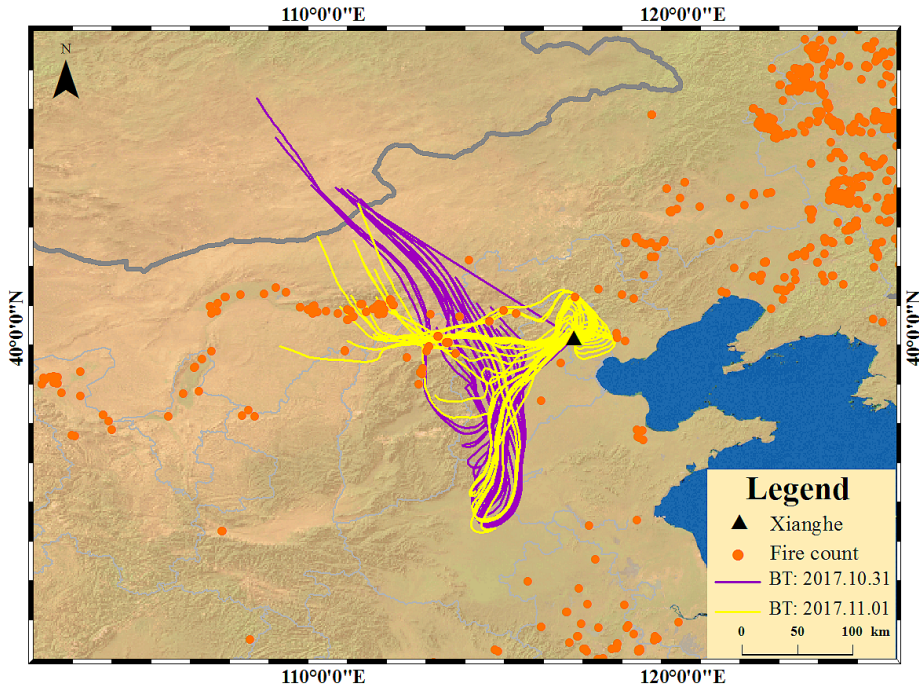
962  
963  
964  
965

**Figure 5.**



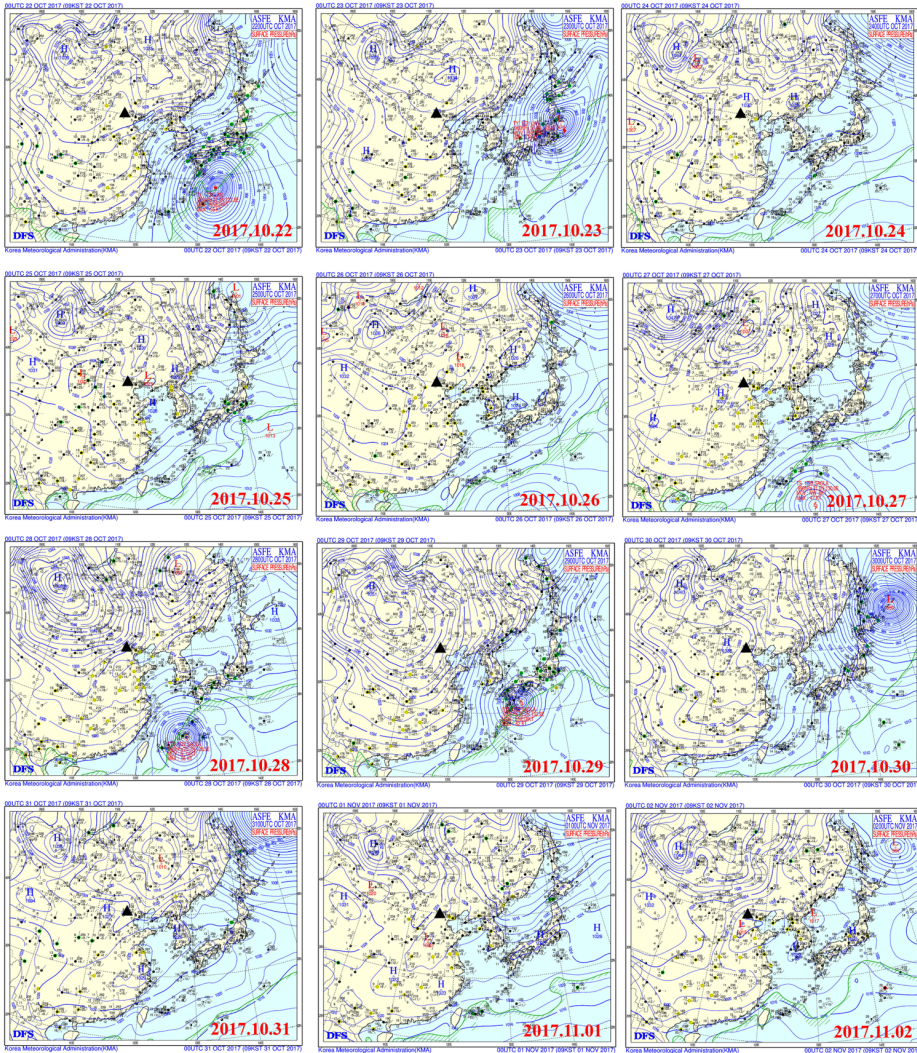
966  
 967  
 968  
 969

**Figure 6.**



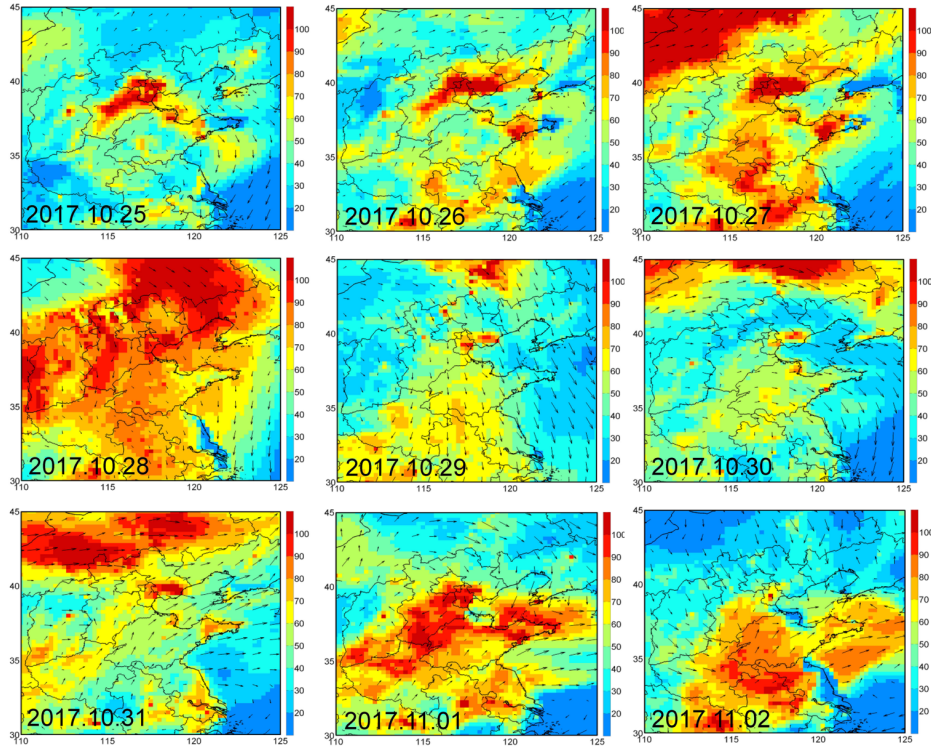
970  
971  
972  
973

**Figure 7.**



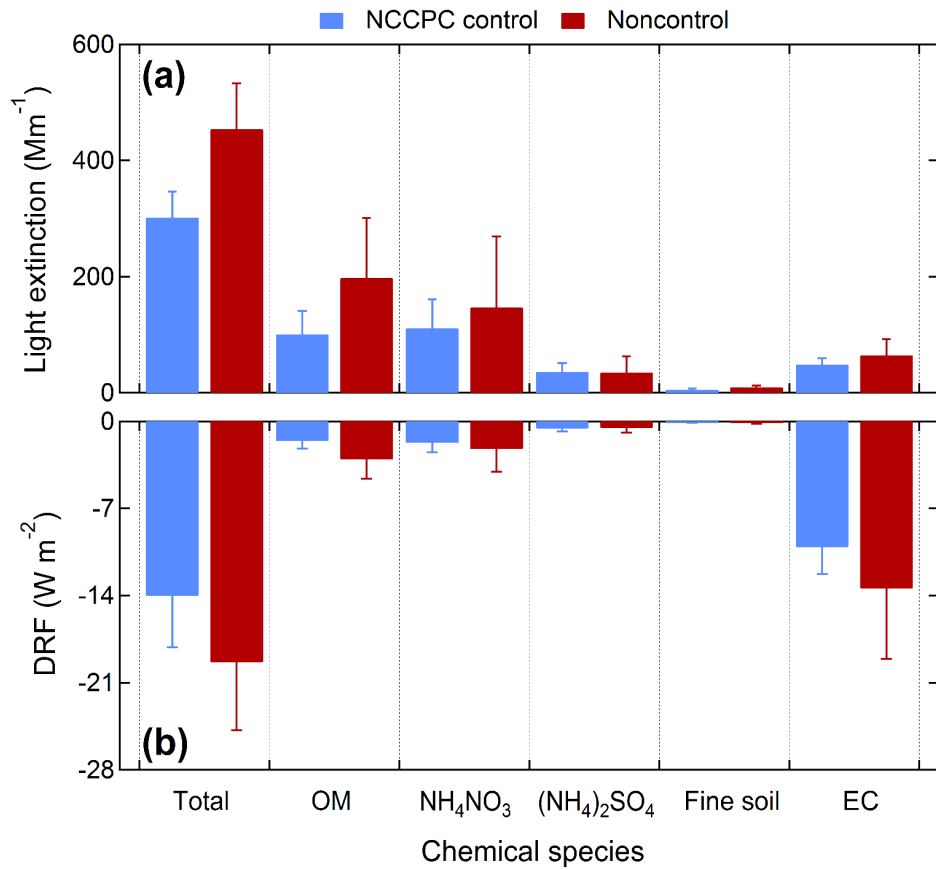
974  
 975  
 976  
 977

**Figure 8.**



978  
979  
980  
981

**Figure 9.**



982  
983

984 **Figure 10.**